



# A Micromachined Vibratory Gyroscope

Qiancheng Zhao, Chunhua He, Jian Cui, and Guizhen Yan

## Contents

Overview .....	422
Structure and Fabrication .....	423
Dynamics Theory .....	425
Drive and Detection Principles .....	430
Drive and Detection with Slide-Film Combs .....	430
Drive and Detection with Squeeze-Film Combs .....	432
Transimpedance Amplifier Detection Method .....	433
Closed-Loop Design for the Drive Mode .....	435
AGC Self-Oscillation Scheme .....	435
AGC + PLL Scheme .....	438
Experimental Tests .....	440
Mode-Matching Control .....	442
Temperature Characteristics Analysis .....	442
Automatic Mode-Matching Control System .....	443
Real-Time Mode-Matching Control System .....	445
Experimental Tests .....	447
Closed-Loop Design for the Sense Mode .....	449
Force Rebalance Control System .....	449
Analysis in the Frequency Domain of Angular Rate .....	451
Analysis in the Frequency Domain of Force .....	452
Experimental Tests .....	453
Temperature Compensation .....	456
Temperature Compensation Principle .....	456
Experimental Test .....	457
Conclusion .....	457
References .....	458

---

Q. Zhao (✉) · C. He · J. Cui · G. Yan  
National Key Laboratory of Science and Technology on Micro/Nano Fabrication, Institute of  
Microelectronics, Peking University, Beijing, China  
e-mail: [zqc@pku.edu.cn](mailto:zqc@pku.edu.cn)

---

**Abstract**

MEMS vibratory gyroscopes are widely used in various fields such as consumer electronics, automotive industry, and navigation systems owing to their merits of low power, low cost, and small volume. A MEMS gyroscope is one of the most important inertial devices, which is researched all over the world.

This chapter will introduce a MEMS vibratory gyroscope, aiming to make more people understand what it is and how it works. Firstly, structure design and fabrication, as well as its dynamics theory, are illustrated. Secondly, closed-loop control for the drive mode and mode-matching control are demonstrated. Finally, closed-loop control for the sense mode, followed by temperature compensation method, is presented in detail. In addition, theoretical deduction, simulation, and experimental tests are combined tightly to make the proposed techniques understand easily.

---

**Keywords**

MEMS gyroscope · Closed-loop control · Mode-matching · Temperature compensation

---

**Overview**

MEMS gyroscopes, which are sensitive to external angular rate, are paid more and more attention from 1980s. According to the performance indice, MEMS gyroscopes can be classified into rate grade, tactical grade, and inertial grade (Yazdi et al. 1998). Rate-grade gyroscopes can be applied to consumer electronics, mobile phones, digital camera, game machines, and wireless mouses. Tactical-grade gyroscopes can be applied to industry control, intelligent automobile, trains, and steamship. Inertial-grade gyroscopes can be applied to satellite, navigation, aerospace, and missile guidance.

There are many kinds of gyroscopes, such as ring laser gyro (RLG), dynamically tuned gyro (DTG), interferometric fiber-optic gyro (IFOG), and MEMS gyro (Yole Developpement 2015, 2016). The performances of RLG or IFOG are far superior to those of MEMS gyro, so there is much work to do for MEMS gyros.

According to incomplete statistics, the universities, companies, and institutes, that research on MEMS gyroscopes, are as follows: Georgia institute of Technology, Standford University, University of Michigan, University of California Berkeley, Irvine, Los Angeles, Middle East Technical University, University of Freiburg, University of Southampton, Seoul National University, Ghent University, Tsinghua University, Peking University, Southeast University, Shanghai Jiaotong University, Zhejiang University, Bosch, ST, InvenSense, NXP, ADI, TI, and so on. Nowadays, the researches on MEMS gyroscopes are focused on the following techniques:

- (1) New material, fabrication, and process (Franssila 2004; Liu et al. 2006; Cho et al. 2013; Shao et al. 2015).
- (2) ASIC monolithic integration (Rombach et al. 2015, 2016).

- (3) High vacuum packaging (Askari et al. 2006; Senkal et al. 2014, 2015; Torunbalci et al. 2015), such as wafer-level packaging.
- (4) New structure and operation principle (Askari et al. 2016; Ahn et al. 2015; Vafanejad and Kim 2015), such as ring, disk, and hemisphere gyroscopes.
- (5) Mode-matching control (Sonmezoglu et al. 2014; He et al. 2013a; Flader et al. 2016), noise suppressing (Lajimi et al. 2017; Sharma 2007; Tatar 2010; Cao et al. 2016; Zihajehzadeh et al. 2015), and coupling signal suppressing (Lee et al. 2008; Acar and Shkel 2005; Cui et al. 2011a).
- (6) Closed-loop control for drive mode (Cui et al. 2011b; Yang and Li 2015; Liu et al. 2014) and force rebalance control for the sense mode (Chen et al. 2016; Rombacha et al. 2015; He et al. 2013b; Tatar et al. 2012).
- (7) Self-calibration (Trusov et al. 2013; Zhang et al. 2015; Aktakka and Najafi 2016) and temperature compensation (Prihodko et al. 2013; Casinovi et al. 2016; Fontanella et al. 2016).
- (8) Reliability test, failure analysis, and reliability design (Li et al. 2014, 2015; Makkonen et al. 2012; Pasquale and Soma 2011; Pierron et al. 2006; Chen et al. 2011).

Aiming at some techniques mentioned above, this chapter will introduce a micromachined vibratory gyroscope.

---

## Structure and Fabrication

The structure design aims to make a gyroscope achieve 1 deg/h bias instability as well as bandwidth larger than 90 Hz. Mode-matching loop will be adopted to reduce the white noise, and closed-loop control for the sense mode will be applied to extend the bandwidth and improve the nonlinearity.

Figure 1 shows the simplified schematic of a Z-axis doubly decoupled tuning fork MEMS vibratory gyroscope, and the chip size is about 5 mm × 3 mm. There are two groups of combs in the drive mode, namely, slide-film drive-sensing combs and slide-film drive combs, which are designed for the closed-loop control of the drive mode. On the other hand, there are three groups of combs in the sense mode, namely, slide-film force feedback combs, squeeze-film sense combs, and squeeze-film mode-matching combs. The sense combs and the force feedback combs are designed for the closed-loop control of the sense mode.

Since slide-film combs can produce a good linear force without inducing the electrostatic stiffness effect, they are suitable for generating the drive force and feedback force. If squeeze-film combs are chosen as the force feedback combs, the resonant frequency of the sense mode would be changed as external Coriolis force, which will increase the complexity of the mode-matching control. Due to a large drive displacement in the drive mode, slide-film combs are applied as the drive-sensing combs to advance the linearity of sense capacitances. Besides, it is beneficial to enhance the quality factor. On the other hand, squeeze-film combs are utilized as the sense combs to improve the detection sensitivity. Meanwhile, thanks to the force

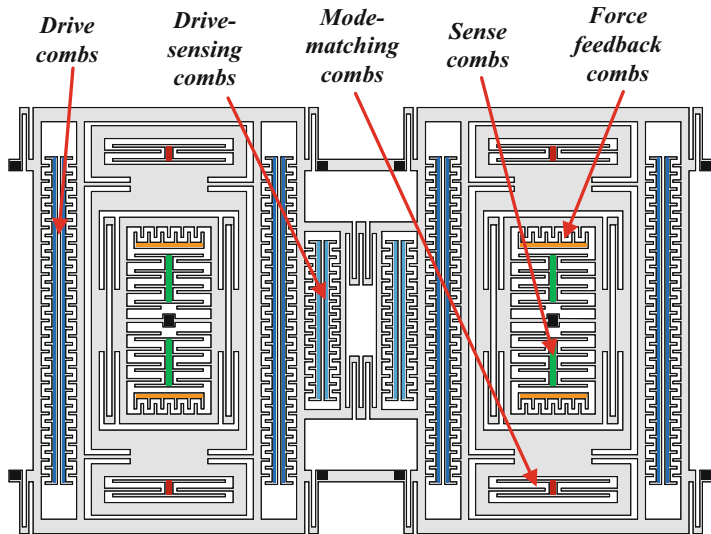
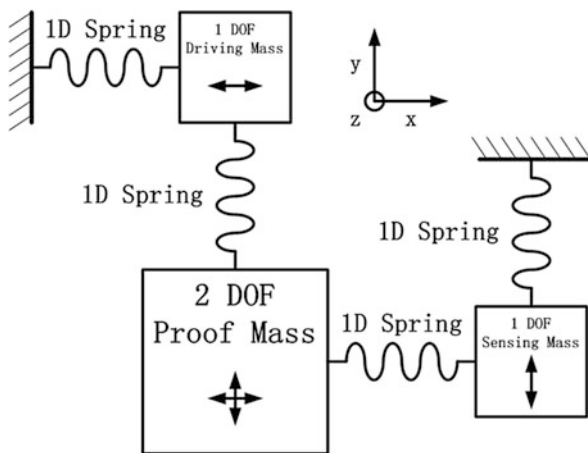


Fig. 1 The schematic of a Z-axis doubly decoupled MEMS tuning fork gyroscope

Fig. 2 The diagram of a doubly decoupled model



rebalance control, the nonlinearity issue induced by squeeze-film combs can be solved. Based on the electrostatic stiffness effect, mode-matching combs can be used to tune the resonant frequency of the drive mode ( $f_d$ ) to equal that of the sense mode ( $f_s$ ).

The diagram of a doubly decoupled model is illustrated in Fig. 2. It figures out that the driving mass and sensing mass have only one degree of freedom (DOF); however, the proof mass has two DOFs. That is to say, the driving mass and proof mass will vibrate along the x-axis when the gyroscope is working, and then the sensing mass and proof mass will vibrate along y-axis when angular rate appears in

z-axis. The Coriolis force is proportional to the displacement and the differential comb capacitance, so transimpedance amplifier can be adopted to fulfill the angular rate detection.

SOG (silicon on glass) process using a silicon/glass wafer bonding and DRIE (deep reactive ion etching) is applied to the fabrication. The initial materials are 4 inch highly doped silicon wafers with the resistivity of 0.01–0.03  $\Omega$  cm and Pyrex 7740 glass whose thermal expansion coefficient matches that of silicon. First, the anchor areas and mechanical moving parts are defined in the silicon substrate by a 20- $\mu$ m deep DRIE etch using silicon dioxide as a mask. A 200-nm Ti/Pt/Au layer is sputtered on the glass wafer and patterned by a lift-off process to form interconnects. Afterward, the two wafers are anodically bonded together, and then the silicon substrate is thinned to about 100  $\mu$ m by KOH etching for 80- $\mu$ m thick device structures. Finally, the gyroscope structure is released by ICP DRIE. More details of the fabrication process can be found in the literature (Li et al. 2000).

## Dynamics Theory

Neglecting the influences of coupling signals, the dynamics equations of the two modes of a MEMS gyroscope can be derived as

$$m_d \ddot{x}(t) + c_d \dot{x}(t) + k_d x(t) = F_0 \sin(\omega t) \quad (1)$$

$$m_s \ddot{y}(t) + c_s \dot{y}(t) + k_s y(t) = -2m_p \Omega v \quad (2)$$

where  $F_d = F_0 \sin(\omega t)$  and  $F_c = -2m_p \Omega v$  are the drive force and Coriolis force, respectively.  $v$  is the drive velocity, and  $\Omega$  is angular rate.  $m_d$ ,  $m_s$ , and  $m_p$  are the drive mass, sense mass, and proof mass, respectively.  $c_d$ ,  $k_d$ , and  $x$  are the damping coefficient, stiffness coefficient, and the displacement of the drive mode, respectively.  $c_s$ ,  $k_s$ , and  $y$  are the damping coefficient, stiffness coefficient, and the displacement of the sense mode, respectively.

Assume that  $\omega_d = \sqrt{\frac{k_d}{m_d}}$  and  $\omega_s = \sqrt{\frac{k_s}{m_s}}$  are the intrinsic radian frequencies of the two modes,  $\xi_d = \frac{c_d}{2m_d \omega_d}$  and  $\xi_s = \frac{c_s}{2m_s \omega_s}$  are the damping ratios of the two modes, and  $Q_d = \frac{1}{2\xi_d}$  and  $Q_s = \frac{1}{2\xi_s}$  are the quality factors of the two modes. Thus, the transfer functions of the two equations above can be expressed as

$$G_d(s) = \frac{x(s)}{F_d(s)} = \frac{1}{m_d s^2 + c_d s + k_d} = \frac{1/m_d}{s^2 + 2\xi_d \omega_d s + \omega_d^2} \quad (3)$$

$$G_s(s) = \frac{y(s)}{F_c(s)} = \frac{1}{m_s s^2 + c_s s + k_s} = \frac{1/m_s}{s^2 + 2\xi_s \omega_s s + \omega_s^2} \quad (4)$$

(1) Since the initial displacement and velocity of the drive mode are both zero, the initial conditions can be written as

$$x(t) = 0, \quad x'(t) = 0 \quad (5)$$

The displacement of the drive mode can be obtained, after solving (1) and (5), as follows

$$x(t) = \frac{\omega A_d}{\omega_d \sqrt{1 - \xi_d^2}} e^{-\frac{\omega_d}{2Q_d} t} \sin \left( \sqrt{1 - \xi_d^2} \omega_d t + \theta_d \right) + A_d \sin (\omega t - \varphi_d)$$

$$A_d = \frac{F_0}{m_d \omega_d^2 \sqrt{\left(1 - \frac{\omega^2}{\omega_d^2}\right)^2 + \left(\frac{\omega}{Q_d \omega_d}\right)^2}} = \frac{F_0/m_d}{\sqrt{\omega^4 + 2(2\xi_d^2 - 1)\omega_d^2 \omega^2 + \omega_d^4}} \quad (6)$$

$$\varphi_d = \operatorname{tg}^{-1} \frac{\omega_d \omega}{Q_d(\omega_d^2 - \omega^2)}, \theta_d = \operatorname{tg}^{-1} \frac{\sqrt{1 - \xi_d^2}}{\xi_d - Q_d(\omega_d^2 - \omega^2)/\omega_d^2}$$

It figures out that the drive displacement includes two parts. One is transient response, while another one is stable response. The former decays exponentially, and the smaller is  $Q_d$ , the larger is the decay speed. The amplitude and phase of the latter are determined by  $\omega_d$  and  $Q_d$ . Closed-loop control of the drive mode aims to obtain stable amplitude of the drive velocity and make the resonant frequency equal the intrinsic frequency. Therefore, it is necessary to detailedly analyze the drive velocity. After taking a derivative of  $x$  with respect to  $t$ , the drive velocity can be yielded as

$$v(t) = \frac{-\omega A_d}{\sqrt{1 - \xi_d^2}} e^{-\frac{\omega_d}{2Q_d} t} \sin \left( \sqrt{1 - \xi_d^2} \omega_d t + \theta_d - \alpha_d \right) + \omega A_d \cos (\omega t - \varphi_d)$$

$$\alpha_d = \operatorname{tg}^{-1} \frac{\sqrt{1 - \xi_d^2}}{\xi_d}$$

Thus, the stable amplitude  $v_d$  can be obtained as

$$v_d = \omega A_d = \frac{F_0/m_d}{\sqrt{[\omega^4 + 2(2\xi_d^2 - 1)\omega_d^2 \omega^2 + \omega_d^4]/\omega^2}} \quad (8)$$

If the denominator reaches minimum,  $v_d$  will be maximum. Assume that

$$h(\omega) = \frac{\omega^4 + 2(2\xi_d^2 - 1)\omega_d^2 \omega^2 + \omega_d^4}{\omega^2} \quad (9)$$

Taking a derivative of  $h(\omega)$  with respect to  $\omega$  yields

$$h'(\omega) = \frac{4\omega^4 - 4\omega_d^4}{\omega^3} \quad (10)$$

Set  $h'(\omega)$  to be zero, we get

$$2(\omega^4 - \omega_d^4)/\omega^3 = 0 \quad (11)$$

Because  $\omega$  is larger than 0, thus

$$\omega = \omega_d \quad (12)$$

$$h(\omega_d) = 4\xi_d^2\omega_d^2 \quad (13)$$

Taking the second derivative of  $h(\omega)$  with respect to  $\omega$  yields

$$h''(\omega) = \frac{2\omega^4 + 6\omega_d^4}{\omega^4} \quad (14)$$

Because

$$h''(\omega_d) = 8 > 0 \quad (15)$$

$h(\omega_d)$  is the minimum when  $\omega > 0$ . Now, the maximum of  $v_d$  is yielded as

$$A_v = v_{d\max} = \frac{F_0}{2\xi_d m_d \omega_d} = \frac{F_0 Q_d}{m_d \omega_d} \quad (16)$$

If  $\omega$  equals  $\omega_d$ ,  $\varphi_d$  is  $90^\circ$ , and the stable drive velocity is

$$v(t) = A_v \sin(\omega_d t) = \frac{F_0 Q_d}{m_d \omega_d} \sin(\omega_d t) \quad (17)$$

(2) As for the sense mode, the angular rate can be defined as

$$-\Omega(t) = -\Omega_R \cos(\omega_R t) \quad (18)$$

Then the Coriolis force can be derived as

$$F_c = -2m_p \Omega v = -2m_p \Omega_R \cos(\omega_R t) A_v \sin(\omega_d t) = -F_{cm} \cos(\omega_R t) \sin(\omega_d t) \quad (19)$$

where  $\omega_R$  is the radian frequency of angular rate and  $F_{cm} = 2m_p A_v \Omega_R$  is the amplitude of  $F_c$ .

(a) If  $\omega_R = 0$ , then  $-\Omega = -\Omega_R$ . Similarly,  $y$  can be deducted as

$$y(t) = \frac{-\omega_d A_s}{\omega_s \sqrt{1 - \xi_s^2}} e^{-\frac{\omega_s}{2Q_s} t} \sin \left( \sqrt{1 - \xi_s^2} \omega_s t + \theta_s \right) - A_s \sin (\omega_d t - \varphi_s)$$

$$A_s = \frac{F_{cm}}{m_s \omega_s^2 \sqrt{\left(1 - \frac{\omega_d^2}{\omega_s^2}\right)^2 + \left(\frac{\omega_d}{Q_s \omega_s}\right)^2}} = \frac{F_{cm}/m_s}{\sqrt{\omega_d^4 + 2(2\xi_s^2 - 1)\omega_s^2 \omega_d^2 + \omega_s^4}} \quad (20)$$

$$\varphi_s = tg^{-1} \frac{\omega_s \omega_d}{Q_s (\omega_s^2 - \omega_d^2)}, \theta_s = tg^{-1} \frac{\sqrt{1 - \xi_s^2}}{\xi_s - Q_s (\omega_s^2 - \omega_d^2)/\omega_s^2}$$

It figures out that the sense displacement includes two parts. One is transient response, while another one is stable response. The former decays exponentially, and the smaller is  $Q_s$ , the larger is the decay speed. The amplitude and phase of the latter are determined by  $\omega_s$  and  $Q_s$ . The larger is  $A_s$ , the bigger is the mechanical sensitivity. Hence, the denominator of  $A_s$  should be minimum. Assume that

$$f(\omega_d) = \omega_d^4 + 2(2\xi_s^2 - 1)\omega_s^2 \omega_d^2 + \omega_s^4 \quad (21)$$

Taking a derivative of  $f(\omega_d)$  with respect to  $\omega_d$  yields

$$f'(\omega_d) = 4\omega_d^3 + 4(2\xi_s^2 - 1)\omega_s^2 \omega_d \quad (22)$$

Setting  $f'(\omega_d)$  to be zero, we get

$$4\omega_d [\omega_d^2 - (1 - 2\xi_s^2)\omega_s^2] = 0 \quad (23)$$

Because  $\omega_d$  is larger than 0, thus

$$\omega_d = \sqrt{1 - 2\xi_s^2} \omega_s = \sqrt{1 - \frac{1}{2Q_s^2}} \omega_s \quad (24)$$

Hence

$$f \left( \sqrt{1 - 2\xi_s^2} \omega_s \right) = 4\xi_s^2 \omega_s^4 (1 - \xi_s^2) \quad (25)$$

Taking the second derivative of  $f(\omega_d)$  with respect to  $\omega_d$  yields

$$f''(\omega_d) = 12\omega_d^2 + 4(2\xi_s^2 - 1)\omega_s^2 \quad (26)$$

Since  $\xi_s$  is often smaller than 0.707,

$$f'' \left( \sqrt{1 - 2\xi_s^2} \omega_s \right) = 8(1 - 2\xi_s^2)\omega_s^2 > 0 \quad (27)$$



Therefore,  $f\left(\sqrt{1-2\xi_s^2}\omega_s\right)$  is the minimum, and the maximum of  $A_s$  is as follows

$$A_{s\max} = \frac{F_{cm}Q_s}{m_s\omega_s^2\sqrt{1-\xi_s^2}} = \frac{F_{cm}Q_s}{m_s\omega_s^2\sqrt{1-1/(4Q_s^2)}} \tag{28}$$

If  $Q_s$  is large enough, we can yield

$$A_{imax} \approx \frac{F_{cm}Q_s}{m_s\omega_s^2} \tag{29}$$

On the other hand, taking a derivative of  $y$  with respect to  $t$ , the sense velocity can be yielded as

$$v_s(t) = \frac{\omega_d A_s}{\sqrt{1-\xi_s^2}} e^{-\frac{\omega_s}{2Q_s}t} \sin\left(\sqrt{1-\xi_s^2}\omega_s t + \theta_s - \alpha_s\right) - \omega_d A_s \cos(\omega_d t - \varphi_s) \tag{30}$$

$$\alpha_s = tg^{-1} \frac{\sqrt{1-\xi_s^2}}{\xi_s}$$

Based on the stable response of sense velocity, the mechanical sensitivity can be defined as

$$S_m = \frac{-\omega_d A_s}{-\Omega_R} = \frac{2m_p A_v \omega_d}{m_s \omega_s^2 \sqrt{\left(1 - \frac{\omega_d^2}{\omega_s^2}\right)^2 + \left(\frac{\omega_d}{Q_s \omega_s}\right)^2}} \tag{31}$$

Similar to the analysis above, if the following condition is met

$$\omega_s = \omega_d, \tag{32}$$

$S_m$  will be largest. That is, the mechanical sensitivity will be maximum after mode-matching control. Thus  $\varphi_s = 90^\circ$ , and

$$A_{vs} = v_{s\max} = \frac{F_{cm}}{2\xi_s m_s \omega_s} = \frac{F_{cm}Q_s}{m_s \omega_s} \tag{33}$$

$$S_{m\max} = \frac{2F_0 m_p Q_d Q_s}{m_d \omega_d m_s \omega_s} \tag{34}$$

$$v_{s\max}(t) = -A_{vs} \sin(\omega_s t) = \frac{-F_{cm}Q_s}{m_s \omega_s} \sin(\omega_s t) = \frac{-2F_0 m_p \Omega_R Q_d Q_s}{m_d \omega_d m_s \omega_s} \sin(\omega_d t) \tag{35}$$

Hence,  $S_m$  can be enlarged by magnifying  $F_0$ ,  $m_p$ ,  $Q_d$ ,  $Q_s$ , and reducing  $m_d$ ,  $m_s$ ,  $\omega_d$ ,  $\omega_s$ . To sum up, as for the stable response of the sense mode, the resonant frequency is  $\sqrt{1 - 2\xi_s^2}\omega_s$  when displacement detection scheme is adopted. However, the resonant frequency is  $\omega_s$ , rather than  $\sqrt{1 - 2\xi_s^2}\omega_s$ , when velocity detection scheme is adopted. Besides, the intrinsic frequency of the two modes can be acquired accurately with velocity detection scheme, and it is immune to the influence of air damping. Hence, in order to achieve better mode-matching, velocity detection scheme should be applied to both drive mode and sense mode.

- (b) The static characteristics of a MEMS gyroscope are depicted in detail when  $\omega_R$  is equal to 0. As for the dynamic characteristics, which means  $\omega_R > 0$ , it will be analyzed in the following section.

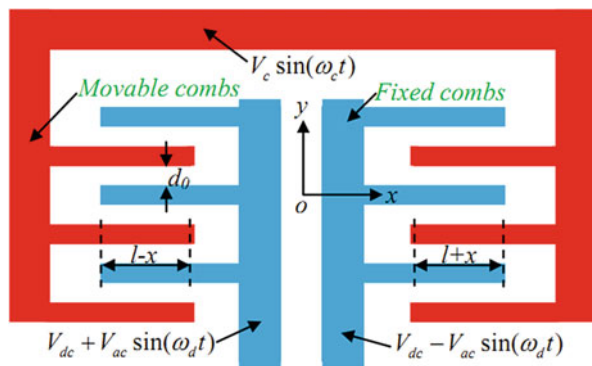
## Drive and Detection Principles

### Drive and Detection with Slide-Film Combs

#### (1) Drive principle

Figure 3 shows the diagram of the slide-film combs. The red parts are fixed and connected to the high-frequency carrier  $V_c \sin(\omega_c t)$ . On the other hand, the blue parts are movable combs and connected to the driving signals  $V_{dc} + V_{ac} \sin(\omega_d t)$  and  $V_{dc} - V_{ac} \sin(\omega_d t)$ .  $V_{dc}$ ,  $V_{ac}$ , and  $V_c$  are the amplitudes of DC, AC, and carrier signals, respectively.  $\omega_c$  often ranges from  $2\pi \times 1$  MHz to  $2\pi \times 10$  MHz, and  $\omega_d$  often ranges from  $2\pi \times 8$  kHz to  $2\pi \times 10$  kHz.  $h$ ,  $l$ ,  $d_0$ ,  $\epsilon$ , and  $N$  are the comb thickness, overlapped length, gap, permittivity, and the number of the comb fingers, respectively.

**Fig. 3** The diagram of the slide-film combs



Thus, the differential voltage between the fixed combs and movable combs are

$$\begin{aligned} V_1 &= V_{dc} + V_{ac} \sin(\omega_d t) - V_c \sin(\omega_c t), V_2 \\ &= V_{dc} - V_{ac} \sin(\omega_d t) - V_c \sin(\omega_c t) \end{aligned} \quad (36)$$

Then we get

$$\begin{aligned} V_1^2 + V_2^2 &= 2V_{dc}^2 + V_{ac}^2 + V_c^2 - [V_{ac}^2 \cos(2\omega_d t) + V_c^2 \cos(2\omega_c t) + 4V_{dc}V_c \sin(\omega_c t)] \\ &- V_2^2 = 4V_{dc}V_{ac} \sin(\omega_d t) - 4V_{ac}V_c \sin(\omega_d t) \sin(\omega_c t) \end{aligned} \quad (37)$$

The potential energies can be expressed as

$$E_1 = \frac{2NV_1^2 \epsilon h(l-x)}{2d_0}, E_2 = \frac{2NV_2^2 \epsilon h(l+x)}{2d_0} \quad (38)$$

Hence, neglecting the high-frequency terms since they will be filtered by the gyroscope, the total driving force is obtained as

$$\begin{aligned} F_{tot} &= F_1 + F_2 = \frac{-\partial E_1}{\partial x} + \frac{-\partial E_2}{\partial x} \\ &= \frac{N\epsilon h(V_1^2 - V_2^2)}{d_0} \underline{\underline{gyro}} \frac{4NV_{dc}V_{ac}\epsilon h \sin(\omega_d t)}{d_0} \end{aligned} \quad (39)$$

Then the electrostatic stiffness, resulted from the derivative of  $F_{tot}$  with respect to  $x$ , can be described as

$$k_x = \frac{-\partial F_{tot}}{\partial x} = 0 \quad (40)$$

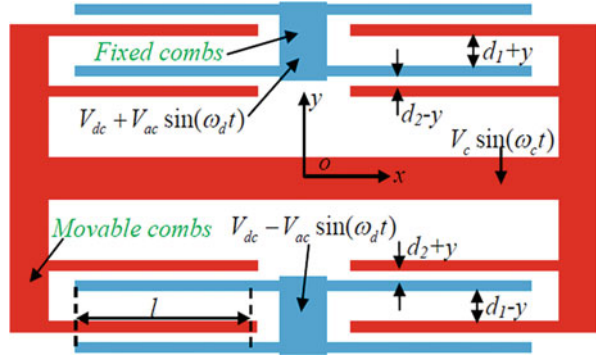
Equation (40) demonstrates that electrostatic stiffness cannot be generated by slide-film combs, so that slide-film combs cannot be used for mode-matching control. However, the driving force possesses good drive linearity since  $F_{tot}$  has nothing to do with  $x$ . Thereby, slide-film combs can be utilized to driving for the two modes.

## (2) Detection principle

Slide-film combs can be also used for displacement or velocity detection. As shown in Fig. 3, removing the drive signal exerted to the fixed combs, they can be utilized to differential capacitance detection. The total differential capacitance  $C_{tot}$  can be derived as

$$C_{tot} = C_{right} - C_{left} = \frac{2N\epsilon h(l+x)}{d_0} - \frac{2N\epsilon h(l-x)}{d_0} = \frac{4N\epsilon h x}{d_0} \quad (41)$$

**Fig. 4** The diagram of the squeeze-film combs



It indicates that  $C_{tot}$  is proportional to the displacement  $x$ , and it possesses good sense linearity. Since the displacement of the drive mode is often large to advance the performances, it requires good sense linearity, and slide-film combs are applicable.

### Drive and Detection with Squeeze-Film Combs

#### (1) Drive principle

Figure 4 shows the diagram of the squeeze-film combs.  $d_1$  and  $d_2$  are the initial gaps of a comb unit. Similarly, the potential energies can be expressed as

$$E_1 = N \left[ \frac{\epsilon h l V_1^2}{2(d_1 + y)} + \frac{\epsilon h l V_1^2}{2(d_2 - y)} \right], E_2 = N \left[ \frac{\epsilon h l V_2^2}{2(d_1 - y)} + \frac{\epsilon h l V_2^2}{2(d_2 + y)} \right] \quad (42)$$

Hence, neglecting the high-frequency terms since they will be filtered by the gyroscope, the total driving force is obtained as

$$\begin{aligned} F_{tot} &= F_1 + F_2 = \frac{-\partial E_1}{\partial y} + \frac{-\partial E_2}{\partial y} \\ &= N \left[ \frac{\epsilon h l V_1^2}{2(d_1 + y)^2} - \frac{\epsilon h l V_1^2}{2(d_2 - y)^2} - \frac{\epsilon h l V_2^2}{2(d_1 - y)^2} + \frac{\epsilon h l V_2^2}{2(d_2 + y)^2} \right] \\ &\approx N \epsilon h l \left( \frac{1}{2d_1^2} - \frac{1}{2d_2^2} \right) (V_1^2 - V_2^2) \underline{\underline{gyro}} 2N \epsilon h l V_{dc} V_{ac} \left( \frac{1}{d_1^2} - \frac{1}{d_2^2} \right) \sin(\omega_d t) \quad (43) \end{aligned}$$

Then the electrostatic stiffness, resulted from the derivative of  $F_{tot}$  with respect to  $y$ , can be described as

$$\begin{aligned}
k_y &= \frac{-\partial F_{tot}}{\partial y} = N \left[ \frac{\varepsilon h l V_1^2}{(d_1 + y)^3} + \frac{\varepsilon h l V_1^2}{(d_2 - y)^3} + \frac{\varepsilon h l V_2^2}{(d_1 - y)^3} + \frac{\varepsilon h l V_2^2}{(d_2 + y)^3} \right] \\
&\approx N \left[ \frac{\varepsilon h l (V_1^2 + V_2^2)}{d_1^3} + \frac{\varepsilon h l (V_1^2 + V_2^2)}{d_2^3} \right] = N \varepsilon h l \left( \frac{1}{d_1^3} + \frac{1}{d_2^3} \right) (V_1^2 + V_2^2) = N \varepsilon h l \left( \frac{1}{d_1^3} + \frac{1}{d_2^3} \right) \\
&\quad \{ 2V_{dc}^2 + V_{ac}^2 + V_c^2 - [V_{ac}^2 \cos(2\omega_d t) + V_c^2 \cos(2\omega_c t) + 4V_{dc} V_c \sin(\omega_c t)] \}
\end{aligned} \tag{44}$$

Equation (43) indicates that  $F_{tot}$  has nothing to do with  $y$ , and the linearity will be affected if  $y$  is large. In addition, Eq. (44) demonstrates that electrostatic stiffness can be generated by squeeze-film combs, so that squeeze-film combs can be used for mode-matching control. However, if they are used to driving, the mode-matching control loop will be affected. Therefore, compared with slide-film combs, squeeze-film combs are not suitable to be used to generate driving force.

The frequency-tuned range is closely related to  $V_{dc}$ ,  $V_{ac}$ ,  $V_c$ ,  $d_1$ ,  $d_2$ ,  $N$ ,  $h$ ,  $l$ , and  $\varepsilon$ , as shown in Eq. (44). If only taking  $V_{dc}$  into account, the electrostatic stiffness can be simplified as

$$k_y = 2V_{dc}^2 N \varepsilon h l \left( \frac{1}{d_1^3} + \frac{1}{d_2^3} \right) \tag{45}$$

Hence, in order to simplify the control scheme, we can only adopt DC voltage to achieve mode-matching control.

## (2) Detection principle

Squeeze-film combs can be also used for displacement or velocity detection. As shown in Fig. 4, removing the drive signal exerted to the fixed combs, they can be utilized to differential capacitance detection. The total differential capacitance  $C_{tot}$  can be derived as

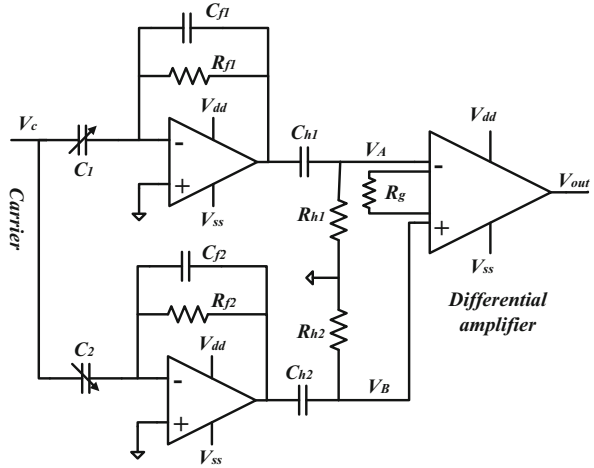
$$\begin{aligned}
C_{tot} &= C_{up} - C_{down} = \left( \frac{N \varepsilon h l}{d_1 + y} + \frac{N \varepsilon h l}{d_2 - y} \right) - \left( \frac{N \varepsilon h l}{d_1 - y} + \frac{N \varepsilon h l}{d_2 + y} \right) \\
&= 2N \varepsilon h l y \left( \frac{1}{d_2^2 - y^2} - \frac{1}{d_1^2 - y^2} \right) \approx 2N \varepsilon h l y \left( \frac{1}{d_2^2} - \frac{1}{d_1^2} \right)
\end{aligned} \tag{46}$$

It indicates that  $C_{tot}$  is proportional to the displacement  $y$ , and it possesses good sense linearity only if  $y$  is small enough. Since the displacement of the sense mode is often small, it requires big sensitivity, and squeeze-film combs are applicable.

## Transimpedance Amplifier Detection Method

The schematic of the readout circuit with transimpedance amplifiers is shown in Fig. 5.  $V_c$  is the carrier signal, which may be a DC or a high-frequency signal.  $V_A$  and

**Fig. 5** The schematic of the readout circuit with transimpedance amplifiers



$V_B$  are the inputs of the differential amplifier.  $C_1$  and  $C_2$  are the differential detection capacitances of a MEMS gyroscope,  $R_{f1}$  and  $R_{f2}$  are the feedback resistors,  $C_{f1}$  and  $C_{f2}$  are the feedback capacitors,  $C_{h1}$  and  $C_{h2}$  are the capacitors of a first-order high pass filter (HPF), and  $R_{h1}$  and  $R_{h2}$  are the resistors of a HPF. According to Fig. 5, we get

$$C_1 = C_{01} + \Delta C_1 \sin(\omega_d t + \alpha) \quad (47)$$

$$C_2 = C_{02} - \Delta C_2 \sin(\omega_d t + \alpha) \quad (48)$$

$$V_A(s) = \frac{-sR_{f1}C_1}{1 + sR_{f1}C_{f1}} \times \frac{sR_{h1}C_{h1}}{1 + sR_{h1}C_{h1}} V_C \quad (49)$$

$$V_B(s) = \frac{-sR_{f2}C_2}{1 + sR_{f2}C_{f2}} \times \frac{sR_{h2}C_{h2}}{1 + sR_{h2}C_{h2}} V_C \quad (50)$$

$$\begin{aligned} V_{out}(s) &= k_g(V_B - V_A) \\ &= k_g V_C \left( \frac{-sR_{f2}C_2}{1 + sR_{f2}C_{f2}} \times \frac{sR_{h1}C_{h1}}{1 + sR_{h1}C_{h1}} - \frac{-sR_{f1}C_1}{1 + sR_{f1}C_{f1}} \times \frac{sR_{h2}C_{h2}}{1 + sR_{h2}C_{h2}} \right) \end{aligned} \quad (51)$$

If  $\Delta C_1 = \Delta C_2 = \Delta C$ ,  $C_{01} = C_{02} = C_0$ ,  $C_{f1} = C_{f2} = C_f$ ,  $R_{f1} = R_{f2} = R_f$ ,  $C_{h1} = C_{h2} = C_h$ ,  $R_{h1} = R_{h2} = R_h$ , and  $1 \ll \omega_d C_h R_h$ , the output can be derived as

$$\begin{aligned} V_{out}(s) &= \frac{2k_g V_C s R_f \Delta C \sin(\omega_d t + \alpha)}{1 + sR_f C_f} \times \frac{sR_h C_h}{1 + sR_h C_h} \\ &\approx \frac{2k_g V_C s R_f \Delta C \sin(\omega_d t + \alpha)}{1 + sR_f C_f} \end{aligned} \quad (52)$$

If  $1 \gg \omega_d C_f R_f$ ,  $V_{out}$  can be simplified as

$$V_{out} = \frac{2k_g V_C s R_f \Delta C \sin(\omega_d t + \alpha)}{1 + s R_f C_f} \approx 2k_g V_C \omega_d R_f \Delta C \cos(\omega_d t + \alpha) \quad (53)$$

It figures out that the phase difference between  $V_{out}$  and  $\Delta C \sin(\omega_d t + \alpha)$  is  $90^\circ$ , and the amplitude has to do with  $\omega_d$ ,  $k_g$ ,  $R_f$ , and  $V_C$ .

### Closed-Loop Design for the Drive Mode

There are two prevalent closed-loop control schemes for the drive mode: AGC (automatic gain control) self-oscillation scheme and AGC + PLL (phase-locked loop) scheme. The stability of these two control system will be deduced below.

#### AGC Self-Oscillation Scheme

Figure 6 illustrates the AGC self-oscillation control loop for the drive mode of a MEMS gyroscope.  $R$  is the setting target,  $A$  is the amplitude of the drive velocity,  $e$  is the control error,  $G$  is the control voltage,  $V_{dc}$  is the driving DC voltage, and  $C(s)$  is the PI (proportion-integration) controller.  $K_{vf}$ ,  $K_{dc}$ , and  $K_{cv}$  are the gains of voltage to force module, displacement to capacitance module, and capacitance to voltage module, respectively.

The key control parameter of the AGC loop is the error between the measured amplitude of the drive velocity and the target. Thus, the aim is to minimize this error and make the system have a swift, accurate, and robust transient response performance. PID (proportion-integration-differentiation) control determines the reaction to the past, current, and future trend of the error and produces a weighted sum of these three actions to adjust the objectives. Usually, the PID controller may be substituted by PI controller since the differentiator circuit may introduce considerable noises. Thereby, PI controller is preferable to employ in this design. The

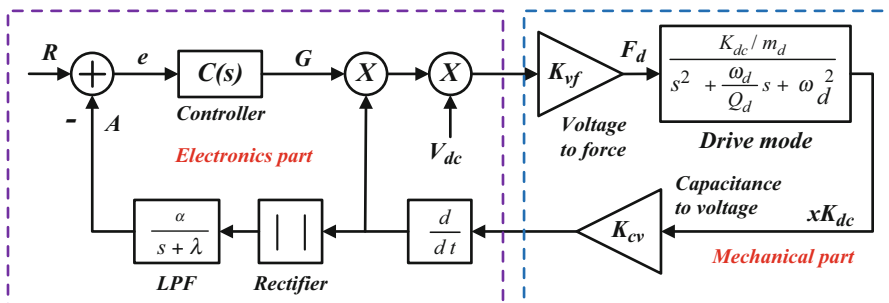


Fig. 6 The AGC self-oscillation control loop for the drive mode of a gyroscope

specific algorithm will be deduced as follows. The transfer function of  $C(s)$  can be written as

$$C(s) = K_p + K_i/s \quad (54)$$

Thus, the plant control equation of the whole loop is formulated as

$$\begin{cases} \ddot{x} + \frac{\omega_d}{Q_d}\dot{x} + \omega_d^2x = \frac{F_d}{m_d} \\ F_d = GK_{vf}V_{dc}K_{dc}K_{cv}\dot{x} \\ \dot{G} = -K_p\dot{A} + K_i(R - A) \\ \dot{A} = |\alpha K_{dc}K_{cv}\dot{x}| - \lambda A \end{cases} \quad (55)$$

From Eq. (55), the dynamic vibration equation can be rewritten as

$$\ddot{x} + \left( \frac{\omega_d}{Q_d} - \frac{GK_{vf}V_{dc}K_{dc}K_{cv}}{m_d} \right) \dot{x} + \omega_d^2x = 0 \quad (56)$$

The aim of the control system is to make the system damping approximate to zero, depending on which the self-oscillation can be realized but not utilizing PLL or other signal generator. Equation (56) illuminated that the AGC control allows the gyroscope to self-oscillate by dynamically adjusting the system's damping. The condition of self-oscillation is  $m_d\omega_d = Q_dGK_{vf}V_{dc}K_{dc}K_{cv}$ . If the measured amplitude is smaller than the desired reference, the AGC system will enlarge the loop gain to reduce the system damping. Conversely, if the oscillation amplitude is large than the reference, the AGC system will add damping to the gyroscope to restrain the amplitude. The gyroscope adjusts itself until the damping of the system is equal to zero, and the system will maintain constant amplitude oscillation. Thus,

$$\ddot{x} + \omega_d^2x = 0. \quad (57)$$

Equation (57) is a linear system with the analytic solution

$$x = u \cos(\omega_d t + \theta) \quad (58)$$

As mentioned above, the controller will minimize the damping value when there is a disturbance in the system. Thus, the damping can be limited to a certain extreme small range, which makes the nonlinear system a weak nonlinear system. In this case, the amplitude and phase of the vibration are both slowly varying parameters with respect to time. From a physical viewpoint, it means that the variation rates of the amplitude and phase are much slower with respect to time. Therefore, the averaging method is feasible to tackle this issue. The essential of the averaging method is to make  $x$  in the nonlinear system of the same form as that in the linear system, such as

$$x = u(t) \cos(\omega_d t + \theta(t)) \quad (59)$$

where  $\theta(t)$  is the phase delay referring to the drive signal and  $u(t)$  is the amplitude. From a mathematical viewpoint, expressing the amplitude and phase as functions of



time is actually equivalent to considering the disturbance caused by the nonlinear terms as a revision for the linear system's solution. Differentiating  $x$  with respect to time yields the velocity

$$\dot{x} = -u\omega_d \sin(\omega_d t + \theta) + \dot{u} \cos(\omega_d t + \theta) - u\dot{\theta} \sin(\omega_d t + \theta) \quad (60)$$

According to the averaging method, the velocity is also expected to have the same form as the position signal. Thereby, the sum of the last two terms can be assumed to be zero (Closkey et al. 2001), namely

$$\dot{u} \cos(\omega_d t + \theta) - u\dot{\theta} \sin(\omega_d t + \theta) \equiv 0. \quad (61)$$

Hence, the velocity can be rewritten as

$$\dot{x} = -u\omega_d \sin(\omega_d t + \theta). \quad (62)$$

The acceleration along the x-axis can be given by differentiating the velocity with respect to time

$$\ddot{x} = -\dot{u}\omega_d \sin(\omega_d t + \theta) - u\omega_d(\omega_d + \dot{\theta}) \cos(\omega_d t + \theta) \quad (63)$$

Applying the averaging method to solve Eq. (55), we can yield the simplified equations

$$\begin{cases} \dot{\bar{u}} = \frac{1}{2}\bar{u} \left( \frac{GK_{vf}V_{dc}K_{dc}K_{cv}}{m_d} - \frac{\omega_d}{Q_d} \right) \\ \dot{\bar{\theta}} = 0 \\ \dot{\bar{A}} = \frac{2}{\pi} \alpha K_{dc}K_{cv}\omega_d \bar{u} - \lambda \bar{A} \\ \dot{\bar{G}} = -K_p \dot{\bar{A}} + K_i (R - \bar{A}). \end{cases} \quad (64)$$

Thus, the equilibrium point of the AGC system can be calculated as

$$\bar{u} = \frac{\pi R \lambda}{2\alpha K_{dc}K_{cv}\omega_d}, \quad \bar{A} = R, \quad \bar{G} = \frac{m_d \omega_d}{K_{dc}K_{cv}K_{vf}V_{dc}Q_d} \quad (65)$$

It shows that the system has a unique equilibrium point and the steady-state error is removed entirely after introducing an integral term. The Jacobian matrix of the nonlinear system at the equilibrium point is represented by

$$J_F(\bar{u}, \bar{A}, \bar{G}) = \begin{bmatrix} 0 & 0 & \frac{\pi R \lambda K_{vf} V_{dc}}{4\alpha m_d \omega_d} \\ \frac{2}{\pi} \alpha K_{dc} K_{cv} \omega_d & -\lambda & 0 \\ -\frac{2}{\pi} \alpha K_{dc} K_{cv} K_p \omega_d & \lambda K_p - K_i & 0 \end{bmatrix} \quad (66)$$

Its characteristic equation is

$$s^3 + \lambda s^2 + \frac{R\lambda K_{cv}K_{dc}K_pK_{vf}V_{dc}}{2m_d}s + \frac{R\lambda K_{cv}K_{dc}K_iK_{vf}V_{dc}}{2m_d} = 0 \tag{67}$$

Based on the Routh–Hurwitz criterion, the linearized system is asymptotically stable only if each coefficient is positive, and the product of the inner two coefficients is larger than that of the outer two (Dorf and Bishop 2005), i.e.,

$$\lambda K_p > K_i \tag{68}$$

Equation (68) means that only if the product of  $\lambda$  and  $K_p$  is larger than  $K_i$ , is the exact solution of the original nonlinear equations convergent to the desired equilibrium point, and the steady-state error gradually reaches around zero.

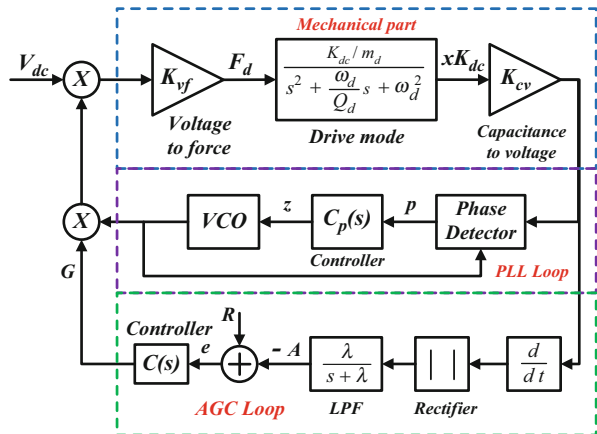
### AGC + PLL Scheme

Figure 7 illustrates the AGC + PLL control loop for the drive mode of a MEMS gyroscope. Different from the former control system, this system includes extra PLL loop, which comprises a phase detector (PD), a controller, and a VCO (voltage-controlled oscillator).  $Y\cos\theta$  is the output of VCO, and the equation of VCO can be expressed as

$$\dot{\theta} = \omega_0 + K_{VCO}z \tag{69}$$

where  $\omega_0, K_{vco}$  are the presetting frequency and tuning gain. The transfer function of PI controller  $C_p(s)$  is

**Fig. 7** The AGC + PLL control loop for the drive mode of a gyroscope



$$C_p(s) = \tau_p + \tau_i/s \tag{70}$$

Assume that the displacement is expressed as

$$x = u(t) \cos(\theta(t) + \varphi(t)) \tag{71}$$

where  $\theta(t) + \varphi(t)$  is the transient phase. Thus, the control equations of the AGC + PLL system can be yielded as

$$\begin{cases} \ddot{x} + \frac{\omega_d}{Q_d} \dot{x} + \omega_d^2 x = \frac{F_d}{m_d} \\ F_d = GK_{vf}V_{dc}y \cos \theta \\ \dot{G} = -K_p \dot{A} + K_i(R - A) \\ \dot{A} = \lambda(|K_{dc}K_{cv}\dot{x}| - A) \\ \dot{\theta} = \omega_0 + K_{VCO}z \\ \dot{z} = \tau_p \dot{p} + \tau_i p \\ \dot{p} = \sigma(K_{dc}K_{cv}xy \cos \theta - p) \end{cases} \tag{72}$$

Applying the averaging method to solve Eq. (72), we can yield the simplified equations as follows:

$$\begin{cases} \dot{\bar{u}} = -\frac{1}{\omega_0 + K_{VCO}\bar{z}} \left[ \frac{\overline{G}K_{vf}V_{dc}y}{2m_d} \sin \bar{\varphi} + \frac{1}{2}\bar{u} \left( K_{VCO}\dot{\bar{z}} + \frac{\omega_d}{Q_d}(\omega_0 + K_{VCO}\bar{z}) \right) \right] \\ \dot{\bar{\varphi}} = -\frac{1}{\omega_0 + K_{VCO}\bar{z}} \left[ \frac{\overline{G}K_{vf}V_{dc}y}{2m_d\bar{u}} \cos \bar{\varphi} + \frac{1}{2} \left( (\omega_0 + K_{VCO}\bar{z})^2 - \omega_d^2 \right) \right] \\ \dot{\bar{G}} = -K_p \dot{\bar{A}} + K_i(R - \bar{A}) \\ \dot{\bar{A}} = \lambda \left[ \frac{2}{\pi} K_{dc}K_{cv}\bar{u}(\omega_0 + K_{VCO}\bar{z}) - \bar{A} \right] \\ \dot{\bar{z}} = \tau_p \dot{\bar{p}} + \tau_i \bar{p} \\ \dot{\bar{p}} = \sigma \left( \frac{1}{2} K_{dc}K_{cv}\bar{u}y \cos \bar{\varphi} - \bar{p} \right) \end{cases} \tag{73}$$

Hence, the equilibrium point of the AGC + PLL system can be calculated as

$$\begin{aligned} \bar{p} = 0, \bar{\varphi} = -\frac{\pi}{2}, \bar{A} = R, \bar{z} = \frac{\omega_d - \omega_0}{K_{VCO}}, \bar{u} = \frac{\pi R}{2K_{dc}K_{cv}\omega_d}, \bar{G} \\ = \frac{\pi R m_d \omega_d}{2K_{dc}K_{cv}K_{vf}V_{dc}Q_d y} \end{aligned} \tag{74}$$

It shows that the system has a unique equilibrium point and the steady-state error is removed entirely after introducing an integral term. The Jacobian matrix of the nonlinear dynamic system at the equilibrium point is represented by

$$\begin{aligned}
 & J(\bar{u}, \bar{\varphi}, \bar{G}, \bar{A}, \bar{p}, \bar{z}) \\
 & = \begin{pmatrix} -\frac{\omega_d}{2Q} & -\frac{\pi^2 R^2 y \sigma K_{vco} \tau_p}{16 K_{cv} K_{dc} \omega_d^3} & \frac{y K_{vf} V_{dc}}{2 m_d \omega_d} & 0 & -\frac{\pi R K_{vco}}{4 Q K_{cv} K_{dc} \omega_d} & -\left( \frac{\pi R K_{vco} (\tau_i - \sigma \tau_p)}{4 K_{cv} K_{dc} \omega_d^2} \right) \\
 0 & -\frac{\omega_d}{2Q} & 0 & 0 & -K_{vco} & 0 \\
 -\frac{2 \lambda K_{cv} K_{dc} K_p \omega_d}{\pi} & 0 & 0 & -K_i + \lambda K_p & -\frac{R \lambda K_p K_{vco}}{\omega_d} & 0 \\
 \frac{2 \lambda K_{cv} K_{dc} \omega_d}{\pi} & 0 & 0 & -\lambda & \frac{R \lambda K_{vco}}{\omega_d} & 0 \\
 0 & \frac{\pi R y \sigma \tau_p}{4 \omega_d} & 0 & 0 & 0 & \tau_i - \sigma \tau_p \\
 0 & \frac{\pi R y \sigma}{4 \omega_d} & 0 & 0 & 0 & -\sigma \end{pmatrix} \quad (75)
 \end{aligned}$$

Equation (75) indicates that its characteristic equation is a sixth-order system, which complicates the analysis. Similar to the solving method above, the stable condition can be calculated. Reader can try to solve it, and we no longer illustrate here.

## Experimental Tests

The AGC control circuit for a MEMS gyroscope is shown in Fig. 8, and it is a pure analog circuit. On the other hand, the AGC + PLL control circuit is illustrated in Fig. 9. It is a mixed signal circuit, and the detection and control algorithms are implemented in FPGA (field-programmable gate array) device. Actually, except for closed-loop control for the drive mode, these two circuits can also accomplish the mode-matching control and force rebalance control. Here, we only take AGC control circuit, for example, to validate the theoretical analysis above.

The transient response of the drive velocity is snatched by a Tektronix TDS2000B oscilloscope, as shown in Fig. 10. The DC component of the drive signal is fixed at

**Fig. 8** The AGC control circuit for a MEMS gyroscope

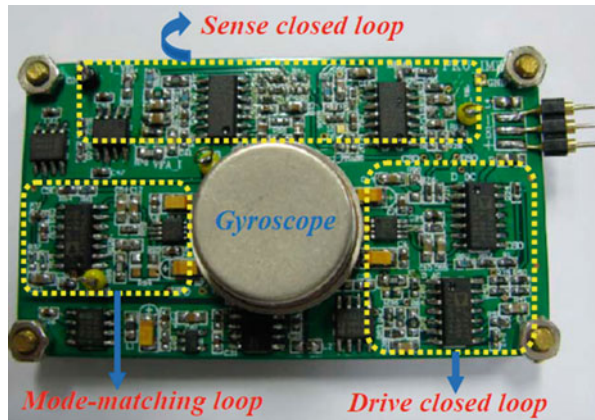


**Fig. 9** The AGC + PLL control circuit for a MEMS gyroscope

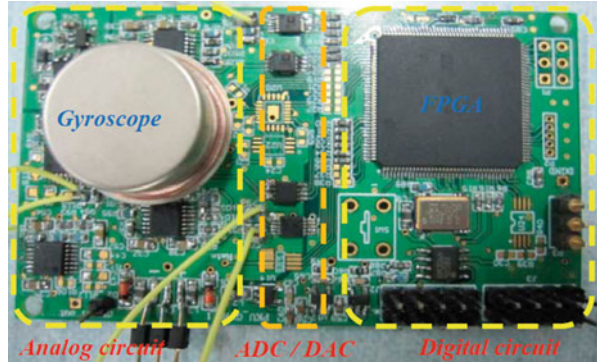
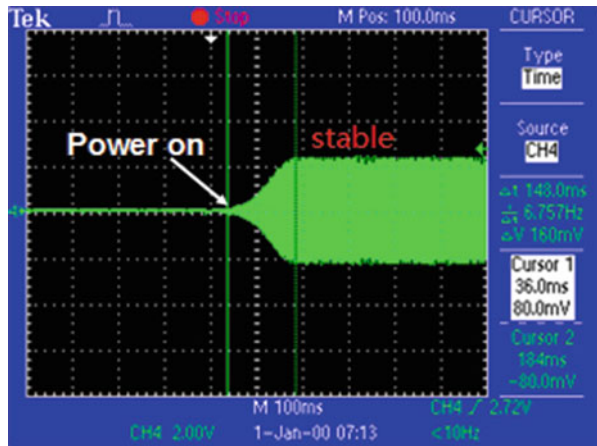


**Fig. 10** The velocity output waveform snatched by a Tek oscilloscope



5 V with automatically adjusting the AC component around 2.5 V. To restrain the circuit noise and filter the harmonic, a first-order LPF is designed with the cutoff frequency 100 Hz. The PI control parameters are set at  $K_i = 90$ ,  $K_p = 16$ , and  $R = 0.2$ . It takes about 150 ms for the gyroscope to self-oscillate to the desired target without obvious overshoot from power-on stage.

Figure 11 shows the drift characteristic of the amplitude of drive velocity for the AGC loop and open loop. Agilent 34401 is used to acquire the amplitude of the drive velocity at one second intervals within an hour. The experiment results demonstrate that the drift range of the open loop is 28.2 mV, which is about 140 times that of AGC-PI control 0.2 mV. The relative fluctuation of velocity amplitude with AGC-PI control is calculated to be about 16.6 ppm, which is reduced by two orders of magnitude compared with the drift of around 4300 ppm in the open loop.

The large fluctuation in the open loop resulted from the slight drift of the resonant frequency of the drive mode and some integrated circuits caused by the temperature rising. During our experiments, we observe that the temperature is not even on the

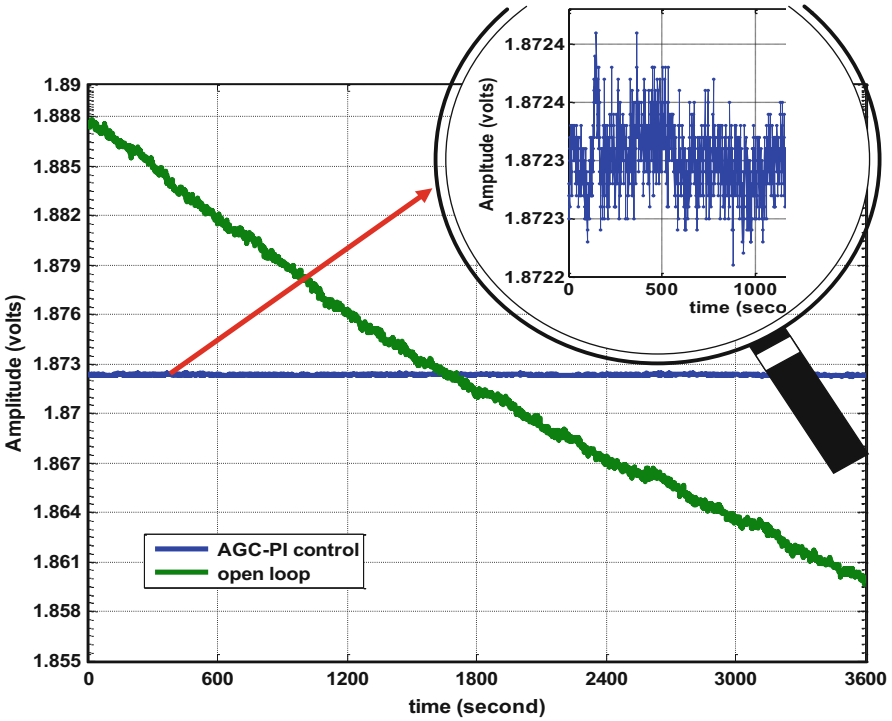


**Fig. 11** Stability of the drive velocity for the AGC loop and open loop

PCB by using a thermal imager since the power consumption is considerable, about 900 mW with  $\pm 15$  V power supply. The frequency drift alters the mechanical gain at the drive frequency point and temperature gradient can affect the performances of the integrated circuits. With AGC control, the resonant frequency and vibration amplitude can be precisely controlled, so the drift of the gyro can be improved substantially. Thus, it is concluded that the proposed AGC control improved the precision and stability of the gyroscope velocity remarkably, which is the fundamental prerequisite of the stability for the angular rate synchronous demodulation in the sense mode.

## Mode-Matching Control

### Temperature Characteristics Analysis

When DC voltage  $V_p$  is exerted to the mode-matching combs, according to Eq. (45), the electrostatic stiffness can be described as:

$$k_e = 2V_p^2 N \epsilon h l \left( \frac{1}{d_1^3} + \frac{1}{d_2^3} \right) \quad (76)$$

Due to mode-matching, the relationship between the two resonant frequencies and  $k_e$  can be expressed as:

$$k_e = 4\pi^2 m_s (f_s^2 - f_d^2) \quad (77)$$

In order to simplify the analysis, here, only take the effect of Young's modulus into account, thus the two resonant frequencies can be written as:

$$f_d(T) = f_{d0} \sqrt{1 - k_{ET}(T - T_0)} \approx f_{d0} \left( 1 - \frac{1}{2} k_{ET}(T - T_0) \right) \quad (78)$$

$$f_s(T) = f_{s0} \sqrt{1 - k_{ET}(T - T_0)} \approx f_{s0} \left( 1 - \frac{1}{2} k_{ET}(T - T_0) \right) \quad (79)$$

where  $f_{d0}$  and  $f_{s0}$  are the corresponding resonant frequencies of the two modes at room temperature  $T_0$ . The temperature coefficient of Young's modulus  $k_{ET}$  is between 25 ppm/ $^{\circ}$ C and 75 ppm/ $^{\circ}$ C. Thus, the frequency difference of the two modes can be derived as:

$$f_s(T) - f_d(T) = (f_{s0} - f_{d0}) \left( 1 - \frac{1}{2} k_{ET}(T - T_0) \right) \quad (80)$$

Since the resonant frequencies vary with ambient temperature  $T$ , it is important to make a real-time mode-matching control. Solving the equations above, the relationship between  $V_p$  and  $f_d$  can be yielded as:

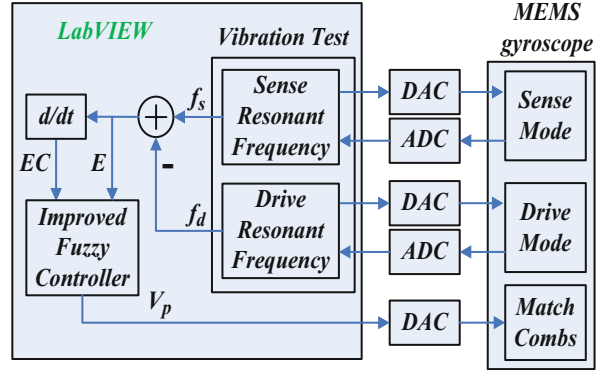
$$V_p(T) = \sqrt{\frac{4(f_{s0}^2 - f_{d0}^2)\pi^2 m_s}{f_{d0}^2 N \epsilon h l \left( \frac{1}{d_1^3} + \frac{1}{d_2^3} \right)}} f_d(T) \quad (81)$$

Equation (81) indicates that if only the temperature effect of the Young's modulus is considered,  $V_p$  is proportional to  $f_d$  and also has an approximately linear dependence on the ambient temperature. In reality,  $V_p$  is not absolutely proportional to  $f_d$ . Other nonideal factors may affect the tuning voltage, such as the variations of gap or overlap areas of the capacitors due to the structural thermal distortion.

## Automatic Mode-Matching Control System

Based on the analysis above, an automatic mode-matching control with improved fuzzy algorithm is proposed, which is illustrated in Fig. 12. It mainly comprises

**Fig. 12** The schematic of the automatic mode-matching control system with improved fuzzy controller



a gyroscope, NI data acquisition card, and LabVIEW software. ADC and DAC represent analog to digital converter and digital to analog converter, respectively. Since the resonant frequencies and quality factors can be measured by vibration test method rapidly and accurately (Yan et al. 2011), the latest match error  $E$  and its differential  $EC$  can be obtained simultaneously. The controlled plant is a complex nonlinear system, so a 2D fuzzy controller can be applied to adjust  $V_p$  according to  $E$  and  $EC$  to achieve mode-matching intelligently.

Fuzzy algorithm is one of the most important intelligent control approaches, which is competent for any nonlinear control system. Owing to the control rapidity and strong robustness with expert experience, it is widely utilized in some gyroscope control systems, such as displacement control and angular rate estimation (Xiao et al. 2009; Fei and Xin 2012). The formula of the traditional incremental fuzzy controller can be expressed as:

$$V_n = V_{n-1} + \Delta V_n = V_{n-1} + \text{fuzzy}(k_p E, k_d EC) \quad (82)$$

where  $V_n$  and  $V_{n-1}$  are the current and the last output of  $V_p$ , and  $\Delta V_n$  is the output increment determined by the fuzzy controller.  $k_p$  and  $k_d$  are the weights of  $E$  and  $EC$ .  $E$ ,  $EC$ , and  $\Delta V_n$  consist of seven language values  $\{nb, nm, ns, ze, ps, pm, pb\}$  on the discourse of  $[-3, 3]$ .  $nb$ ,  $nm$ ,  $ns$ ,  $ze$ ,  $ps$ ,  $pm$ , and  $pb$  represent negative big, negative medium, negative small, zero, positive small, positive medium, and positive big, respectively. The rule table is the core which is set based on expert experience. The rules are established referring to the following principles: (1) If  $E$  and  $EC$  are large,  $\Delta V_n$  should be adjusted to rapidly reduce the error. (2) If  $E$  and  $EC$  are small,  $\Delta V_n$  should be tuned to restrain overshoot and eliminate static error. For example, if  $E$  is  $nb$  and  $EC$  is  $nb$ , then  $\Delta V_n$  is  $pb$ . If  $E$  is  $nb$  and  $EC$  is  $pb$ , then  $\Delta V_n$  is  $ze$ .

The traditional fuzzy controller can be regarded as a nonlinear PD controller, as shown in Eq. (82), which will result in a nonideal control precision due to the lack of an integration term. According to classical control theory, the control static error cannot be eliminated without an integration term. Therefore, traditional fuzzy



algorithm should be improved by introducing an integration term  $k_i E$  to achieve a better control effect, as depicted below.

$$V_n = V_{n-1} + \Delta V_n = V_{n-1} + \text{fuzzy}(k_p E, k_d EC) + k_i E \quad (83)$$

According to the fuzzy rules and Mamdani algorithm, a look-up table (LUT) for fuzzy control can be yielded with the following formula.

$$\Delta V_n' = \bigcup_{i=1}^{49} (E' \text{ and } EC') \circ [(E_i \text{ and } EC_i) \rightarrow \Delta V_{ni}] \quad (84)$$

where  $E'$  and  $EC'$  are the typical inputs of  $E$  and  $EC$ .  $E_i$ ,  $EC_i$ , and  $\Delta V_{ni}$  are the fuzzy rules of fuzzy sets. Afterward, centroid method is used for defuzzification of  $\Delta V_n'$  to obtain  $\Delta V_n$ . Finally, the control LUT can be stored in the memory to save computing time, which simplifies the realization in LabVIEW or other devices.

The improved fuzzy controller can be considered as the combination of traditional fuzzy controller and PID controller, which makes it possess good control speed, strong robustness, and high control precision.

This novel automatic mode-matching method scarcely depends on the  $Q_s$  and is hardly affected by the uncertain parasitic phase shift induced by the readout circuits. Besides, improved fuzzy algorithm and vibration test theory are adopted to the feedback control loop, which will enhance the control precision and rapidity. Furthermore, this method can be easily realized.

## Real-Time Mode-Matching Control System

The automatic mode-matching method depicted in Fig. 12 is still a once-time control method, and it will fail to work when Coriolis force comes into being since vibration test must work offline. However, it can be applied to obtain the corresponding  $f_d$  and  $V_p$  rapidly under a few different temperature points. Then BP (back propagation) neural network algorithm is adopted to study the relationship between  $f_d$  and  $V_p$  based on those measured data and make a prediction afterwards. Since  $f_d$  changes with ambient temperature and can be monitored in the drive closed-loop, it can be used as a temperature feedback variable and applied to real-time mode-matching control and online temperature compensation. Thus,  $V_p$  varies with  $f_d$  when ambient temperature changes, which achieves a real-time mode-matching control, as shown in Fig. 13.

Neural network algorithm is another important intelligent control approach, which can acquire the experience from some training data and then accomplish the control or prediction well. Since it possesses the strong ability of generalization, self-adaption, and nonlinear mapping for the nonlinear or uncertain system, it is usually adopted to the temperature compensation for some MEMS devices (Zhang et al. 2009; Yang et al. 2010).

In this chapter, a three-layer BP neural network will be utilized for the real-time prediction control, as shown in Fig. 14.  $X$  is the input matrix of input layer, and  $Y, Z$

**Fig. 13** The schematic of the real-time mode-matching control system with neural network controller

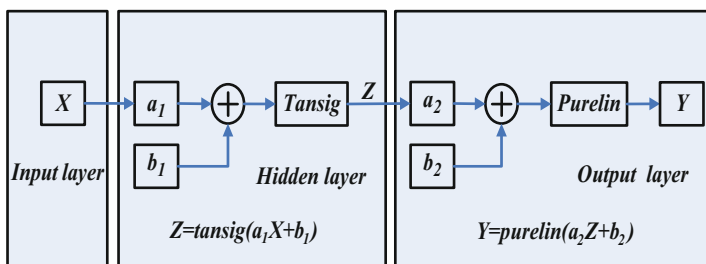
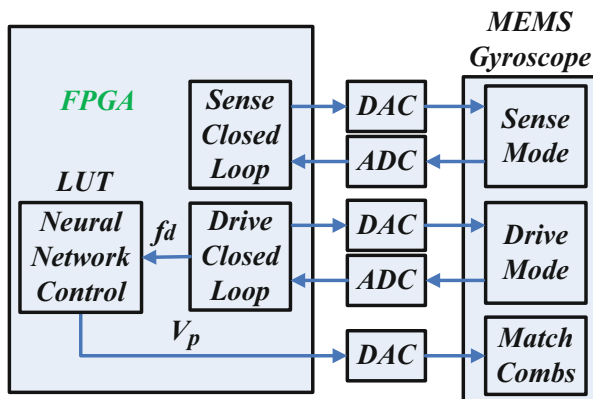


**Fig. 14** The architecture of a three-layer BP neural network controller

are the output matrices of hidden layer and output layer, respectively. Tansig and pureline functions are utilized as the transfer functions of the hidden layer and output layer, respectively. Trainlm (Levenberg–Marquardt algorithm) function is utilized for network training, and mean square error is used as the performance estimation function. In the study process, the weights matrices  $a_1, a_2$  and the threshold matrices  $b_1, b_2$  are adjusted with steepest descent method to make the training error ( $ER$ ) meet the expected target.

$$ER = (Y - Tar)' \times (Y - Tar) / 2 \tag{85}$$

where  $Tar$  is the expected output matrix used for the training. After the training with the acquired data,  $a_1, a_2$  and  $b_1, b_2$  are confirmed. Then the BP neural network can be used to make a prediction according to the inputs.

Neural network algorithm is so complex that it will occupy much calculating time and vast hardware resources, but this calculation can be accomplished by Matlab software beforehand. Similarly, a LUT of the relationship between  $f_d$  and  $V_p$  is generated by Matlab and stored in the ROM of FPGA device, which will simplify the realization.

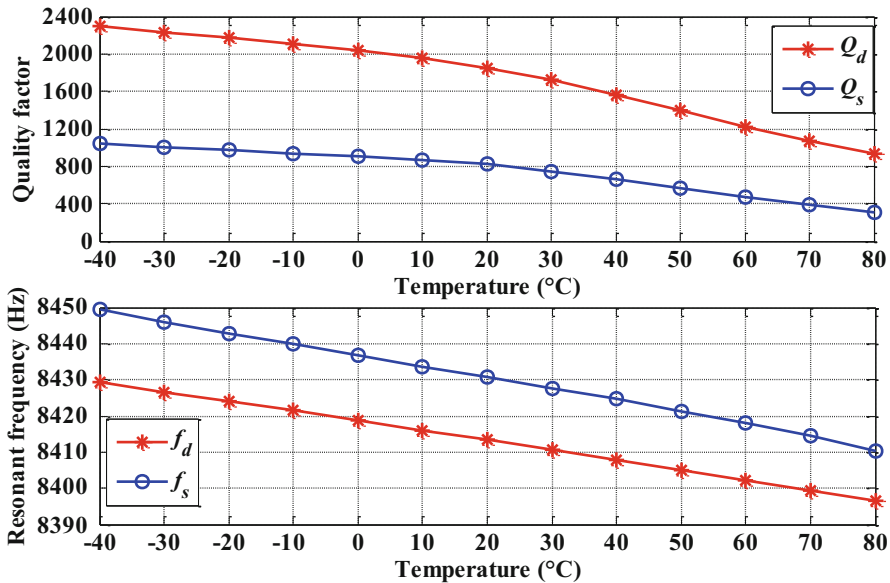


**Fig. 15** The resonant frequencies and quality factors of the two modes both vary with the ambient temperature

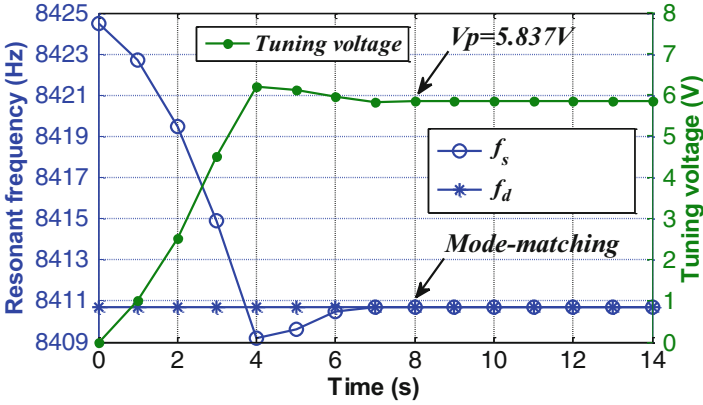
### Experimental Tests

The test circuit for a vacuum packaging gyroscope is mounted on the rate table in an oven chamber. The temperature of the oven chamber is configured from  $-40\text{ }^{\circ}\text{C}$  to  $80\text{ }^{\circ}\text{C}$ . We conduct the tests per  $10\text{ }^{\circ}\text{C}$ , and every temperature point is kept for about 30 min to make the gyroscope’s temperature identical with ambient temperature.

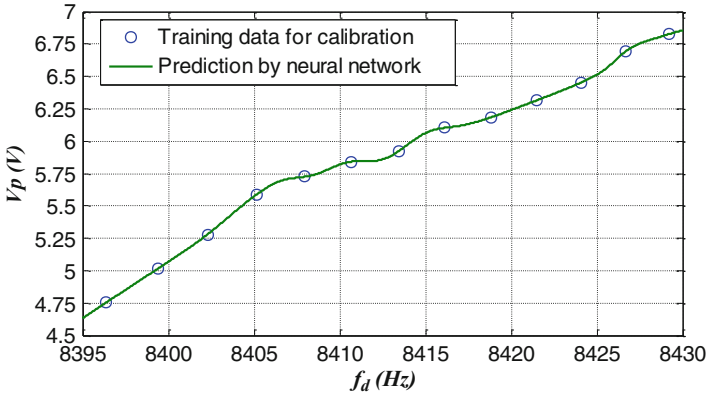
Experimental results indicate that both  $f_s$  and  $f_d$  vary with ambient temperature nearly linearly, and the change is about 35 Hz over the full temperature range, as shown in Fig. 15. But their slopes are different, which will induce some match error in the once-time mode-matching control system. Thus, mode-matching voltage should trace with ambient temperature real-time. On the other hand, due to the increasing thermal damping, both  $Q_s$  and  $Q_d$  drop fast and nonlinearly as temperature increases, as shown in Fig. 15.  $Q_s$  is always smaller than  $Q_d$  because there are so many squeeze-film combs in the sense mode.

Figure 16 demonstrates that  $f_s$  changes with tuning voltage as time goes on. It only needs about 8 s to achieve mode-matching automatically in the improved fuzzy control system, which testifies the automatic mode-matching control system is feasible, rapid, and accurate. The mode-matching voltage is measured to be 5.837 V when ambient temperature is  $30\text{ }^{\circ}\text{C}$ . After mode-matching control, the resonant frequencies of the two modes are both 8410.69 Hz.

Therefore, the automatic mode-matching control system is proved effective to obtain the corresponding  $f_d$  and  $V_p$  when ambient temperature is constant. Thirteen groups of data about  $f_d$  and  $V_p$  can be yielded with the fuzzy control system under 13



**Fig. 16** Improved fuzzy control for automatic mode matching control when ambient temperature is set 30 °C



**Fig. 17** The relationship between the drive resonant frequency and the mode-matching voltage

different temperatures configured from  $-40\text{ }^{\circ}\text{C}$  to  $80\text{ }^{\circ}\text{C}$ , as marked with 13 blue circles in Fig. 17. Then neural network algorithm is applied to study the relationship between  $f_d$  and  $V_p$  based on those data, and make a prediction, as shown in the green curve in Fig. 11. It indicates that the relationship between  $f_d$  and  $V_p$  is nonlinear, which will be used for the real-time mode-matching control.

In the once-time mode-matching control system,  $V_p$  is a constant, for instance,  $V_p$  is set to be 5.837 V, thus the gyroscope can maintain mode-matching only if the ambient temperature is  $30\text{ }^{\circ}\text{C}$ . The matching error is larger than 6 Hz over the temperature range from  $-40\text{ }^{\circ}\text{C}$  to  $80\text{ }^{\circ}\text{C}$ , as depicted in the blue curve in Fig. 18. On the other hand, the matching error can be restrained to be smaller than 0.32 Hz in the full temperature range in the real-time mode-matching control system, as illustrated in the red curve in Fig. 18. The control precision is improved by more than one order of magnitude, which is enough for a gyroscope with  $Q_s$  less than 1200.

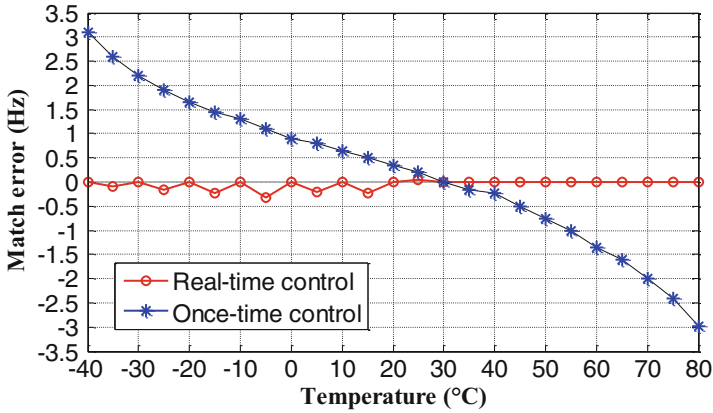


**Fig. 18** The relationships between the mismatched frequency and temperature in two control systems

## Closed-Loop Design for the Sense Mode

### Force Rebalance Control System

The force rebalance control system for the sense mode of a gyroscope is shown in Fig. 19. There are two closed loops in the system due to the demodulation and remodulation components, namely Coriolis force rebalance control loop and quadrature rebalance control loop. Given the completeness, the demodulation and remodulation signals of the two loops should be orthogonal. A HPF is adopted to eliminate the DC signal, and a LPF is used to suppress the high frequency signal. After G-PI control, a remodulation process is required to construct the feedback force to balance the external forces. Then  $y_i(t)$  and  $y_q(t)$  are used as the final outputs of the closed-loop system.  $-\Omega(t)$  and  $q(t)$  are the input angular rate and equivalent coupling signal, respectively.  $\theta$  is the demodulation phase.  $F_s$  is the total force exerted to the sense mode.  $F_c$ ,  $F_q$ , and  $F_b$  represent Coriolis force, quadrature force, and feedback force, respectively.  $m_p A_v$ ,  $k_{qf}$ , and  $k_{vf}$  are the corresponding force coefficients of them. If  $m_p A_v = k_{qf} = k_{vf}$ ,  $y_i(t)$  and  $y_q(t)$  will equal  $-\Omega(t)$  and  $q(t)$  after force rebalance, respectively.

In literature (Sonmezoglu et al. 2012; Tatar et al. 2012), the closed-loop analysis is mainly conducted in the frequency domain of angular rate ( $f_r$  domain). However, it is still not enough without the analysis in the frequency domain of force ( $f$  domain). Strictly, the closed loop is a force rebalance control system, instead of an angular rate feedback system, thus the stability analysis results in  $f$  domain will be more interesting and accurate. Through the demodulation or modulation process, signals can be transferred between  $f$  domain and  $f_r$  domain. Here, the stability analysis of the control system in both  $f_r$  domain or  $f$  domain will be conducted.

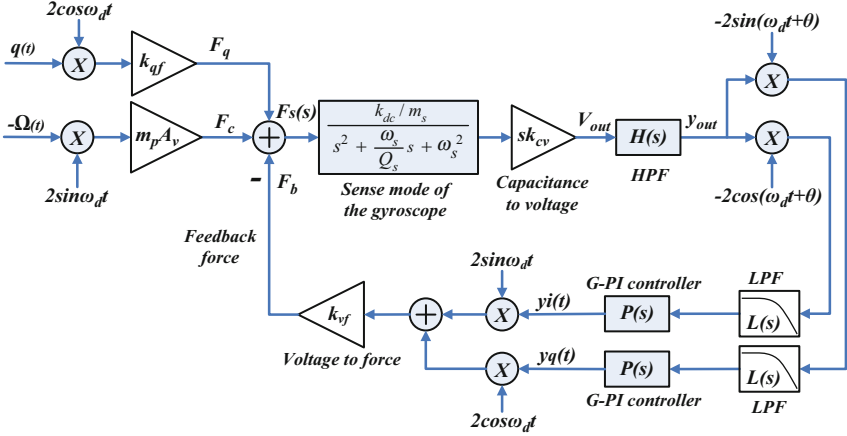


**Fig. 19** Block diagram of the force rebalance control system for the sense mode of a MEMS gyroscope

The transfer functions of sense mode of the gyroscope  $G_s(s)$ , HPF  $H(s)$ , LPF  $L(s)$ , and G-PI controller  $P(s)$  are expressed as follows

$$G_s(s) = \frac{k_{dc}}{m_s s^2 + c_s s + k_s} = \frac{k_{dc}/m_s}{s^2 + s\omega_s/Q_s + \omega_s^2} \tag{86}$$

$$H(s) = \frac{s}{s + \omega_h} \tag{87}$$

$$L(s) = \frac{\omega_l^2}{s^2 + 2\xi_l \omega_l s + \omega_l^2} \tag{88}$$

$$P(s) = \frac{k_p(s + \omega_2)}{(s + \omega_1)(s + \omega_3)} \tag{89}$$

where  $\omega_h$  is the cutoff frequency of the first-order HPF.  $\xi_l$  and  $\omega_l$  are the damping ratio and center frequency of the second-order LPF, respectively.  $(s + \omega_2)/(s + \omega_1)$  can be considered as a PI controller or a lag compensator, and  $k_p/(s + \omega_3)$  is a first-order LPF applied to eliminate the high-frequency components. Because the useful force signals locate within a narrow band around  $\omega_d$ , there is no need to fulfill a wide-band force control for making the controller design easier. Thereby, narrow-band force feedback control is adopted.

In  $f_r$  domain,  $s = j\omega_R = j2\pi f_r$ , while in  $f$  domain,  $s = j\omega = j2\pi f$ . The deductions in the two domains will be conducted.

### Analysis in the Frequency Domain of Angular Rate

The two loops in Fig. 19 are similar to each other, which can not only guarantee the same bandwidth of them but also simplify the design of the controllers. Here, only take the Coriolis force control loop, for example, to fulfill the deduction. Block diagram of the open loop system for angular rate is shown in Fig. 20. After a series of deductions in  $f_r$  domain and filtering the high-frequency terms, the transfer function of the open loop system  $D_r(s)$  can be derived as

$$D_r(s) = \frac{y_i(s)}{-\Omega(s)} = -jm_p A_v k_{cv} \left[ \frac{(s - j\omega_d)e^{j\theta} G_s(s - j\omega_d) H(s - j\omega_d) - (s + j\omega_d)e^{-j\theta} G_s(s + j\omega_d) H(s + j\omega_d)}{(s + j\omega_d)e^{-j\theta} G_s(s + j\omega_d) H(s + j\omega_d)} \right] L(s)P(s) \quad (90)$$

Thus, the closed-loop transfer function  $T_r(s)$  and sensitivity transfer function  $S_r(s)$  can be defined as follows

$$T_r(s) = \frac{D_r(s)}{1 + D_r(s)} \quad (91)$$

$$S_r(s) = \frac{1}{1 + D_r(s)} \quad (92)$$

When mode-matching,  $\omega_d = \omega_s$ , which is often larger than  $2\pi \times 8$  kHz.  $\omega_h$  is set to be  $2\pi \times 80$  Hz, so  $\omega_d \gg \omega_h$ . The bandwidth (BW) of a MEMS gyroscope is often smaller than 200 Hz, thus  $2\omega_s \gg \omega_R$ . In mode-matching,  $\theta$  is set to be  $90^\circ$ . Assume that  $\omega_t = \omega_s/(2Q_s)$ , then the original mechanical response  $SF_m(s)$  can be derived from  $D_r(s)$  when the term  $L(s)P(s)$  is neglected, as follows

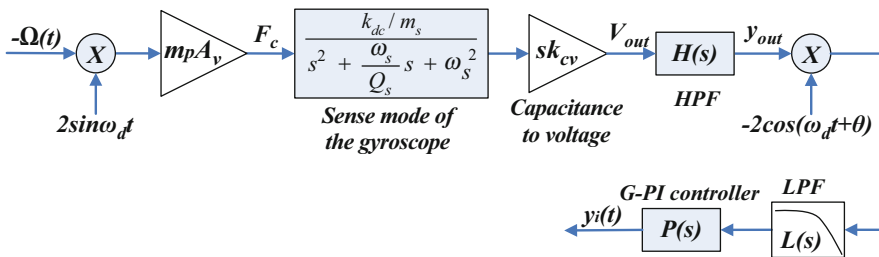


Fig. 20 Block diagram of the open loop system for angular rate

$$\begin{aligned}
SF_m(s) &= -jm_p A_v k_{cv} \left[ (s-j\omega_d) e^{j\theta} G_s(s-j\omega_d) H(s-j\omega_d) - (s+j\omega_d) e^{-j\theta} G_s(s+j\omega_d) H(s+j\omega_d) \right] \\
&= -jm_p A_v k_{cv} \left[ j(j\omega_R-j\omega_d) \times \frac{k_{dc}/m_s}{\omega_s^2 - (\omega_R-\omega_d)^2 + j(\omega_R-\omega_d)\omega_s/Q_s} \times \frac{j(\omega_R-\omega_d)}{j(\omega_R-\omega_d) + \omega_h} \right. \\
&\quad \left. + j(j\omega_R+j\omega_d) \times \frac{k_{dc}/m_s}{\omega_s^2 - (\omega_R+\omega_d)^2 + j(\omega_R+\omega_d)\omega_s/Q_s} \times \frac{j(\omega_R+\omega_d)}{j(\omega_R+\omega_d) + \omega_h} \right] \\
&\approx \frac{m_p A_v k_{cv} k_{dc}}{m_s} \left[ \frac{j(\omega_R-j\omega_d)}{(2\omega_s-\omega_R)\omega_R - j(2\omega_s-2\omega_R)\omega_t} - \frac{j(\omega_R+j\omega_d)}{(2\omega_s+\omega_R)\omega_R - j(2\omega_s+2\omega_R)\omega_t} \right] \\
&\approx \frac{m_p A_v k_{cv} k_{dc}}{m_s} \left[ \frac{j(\omega_R-j\omega_s)}{2\omega_s(\omega_R-j\omega_t)} - \frac{j(\omega_R+j\omega_s)}{2\omega_s(\omega_R-j\omega_t)} \right] = \frac{m_p A_v k_{cv} k_{dc}}{m_s(j\omega_R+\omega_t)} = \frac{m_p A_v k_{cv} k_{dc}}{m_s(s+\omega_t)}
\end{aligned} \tag{93}$$

It demonstrates that  $SF_m(s)$  is a first-order system whose cutoff frequency is  $\omega_t$ . Meanwhile, the original bandwidth is  $BW = \omega_t = \omega_s/(2Q_s)$ . After vacuum packaging,  $Q_s$  is larger than 500, which means BW will be smaller than 10 Hz. Thereby, in order to meet more application demands, BW of a mode-matching gyroscope should be extended by the force rebalance control. The scale factor of a MEMS gyroscope with closed-loop controlled sense mode can be expressed as

$$SF_{closed} = \frac{y_i(t)}{-\Omega(t)} = \frac{m_p A_v}{k_{vf}} \tag{94}$$

Since  $k_{vf}$ ,  $A_v$ , and  $m_p$  hardly vary with ambient temperature, compared with Eq. (31) of the open-loop system, the temperature sensitivity of the scale factor of the closed-loop system is improved. In addition, after force rebalance, the sense combs are kept in the equilibrium position, which will improve the nonlinearity and enhance the measured range. The bandwidth can be also changed flexibly by tuning the parameters of the G-PI controller. In general, the performances of a force rebalance control system are superior to those of an open-loop system.

## Analysis in the Frequency Domain of Force

Block diagram of the open-loop system for external force is illustrated in Fig. 21. After a series of deductions in  $f$  domain and filtering the high-frequency terms, the transfer function of the open-loop system  $D(s)$  can be easily derived as

$$\begin{aligned}
D(s) &= \frac{F_b(s)}{F_s(s)} \\
&= 2j s k_{cv} k_{vf} \left[ e^{-j\theta} L(s-j\omega_d) P(s-j\omega_d) - e^{j\theta} L(s+j\omega_d) P(s+j\omega_d) \right] H(s) G_s(s)
\end{aligned} \tag{95}$$



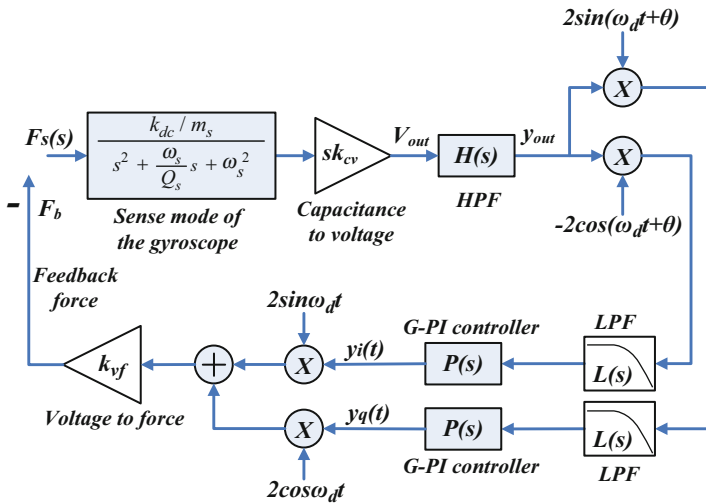


**Fig. 21** Block diagram of the open loop system for external force

Thus, the closed-loop transfer function  $T(s)$  and sensitivity transfer function  $S(s)$  can be defined as follows

$$T(s) = \frac{D(s)}{1 + D(s)} \tag{96}$$

$$S(s) = \frac{1}{1 + D(s)} \tag{97}$$

Hence, the frequency responses in  $f_r$  domain and  $f$  domain can be simulated by Matlab with Eqs. (86)–(97). The key parameters of filters and G-PI controller are finally set according to simulation results and stability indices. In the experimental tests, a virtual rate-table method (Cui et al. 2012) can be adopted to obtain the frequency responses and validate the theoretical analysis.

### Experimental Tests

Here, we take a mode-matching MEMS gyroscope, for example, to realize the force rebalance control. After mode-matching control, the resonant frequencies of the two modes are both 8410.6 Hz at room temperature, and  $Q_s$  is about 750.

The experimental frequency responses of  $D_r(s)$ ,  $T_r(s)$ ,  $S_r(s)$ , and  $SF_m(s)$  are depicted in Figs. 22 and 23. From these two diagrams, the phase margin ( $PM$ ), gain margin ( $GM$ ), cutoff frequencies ( $f_c$ ), sensitivity margins ( $M_s$ ), and bandwidth ( $BW$ ) can be calculated, as listed in Table 1.

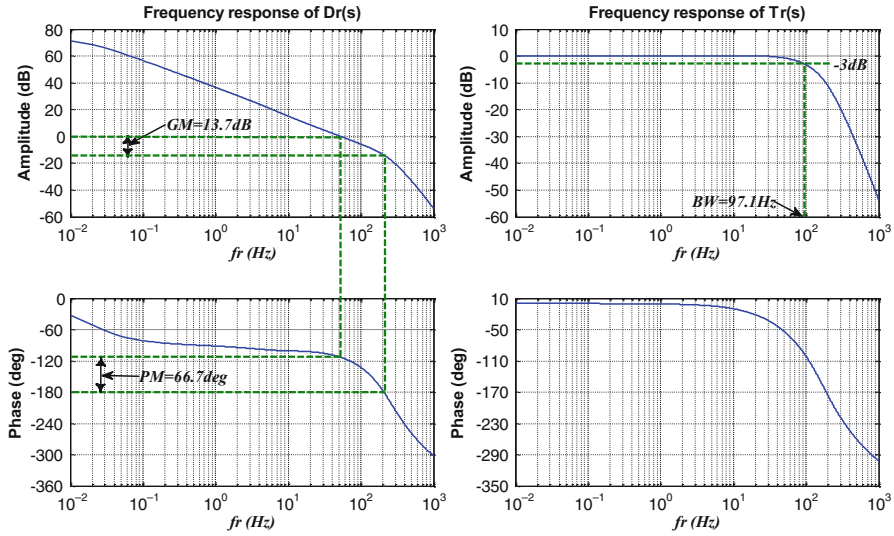


Fig. 22 Frequency responses of  $D_r(s)$  and  $T_r(s)$

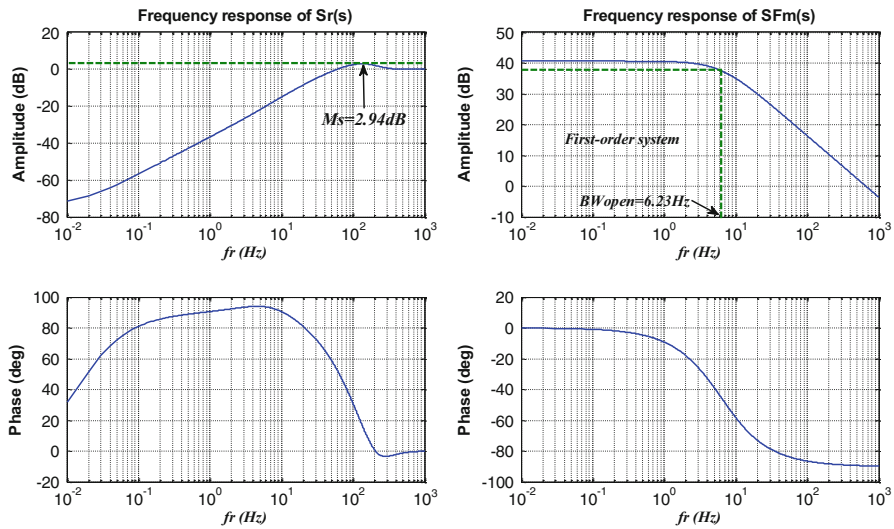
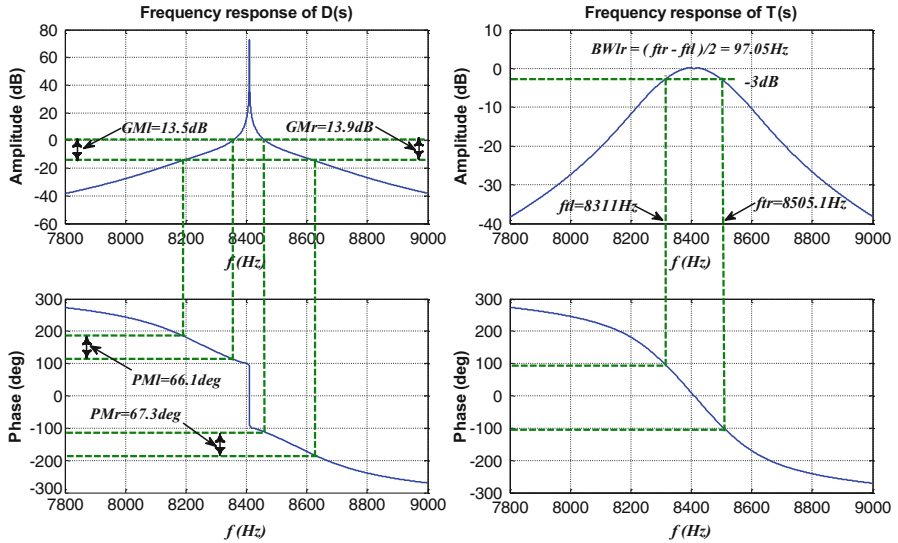


Fig. 23 Frequency responses of  $S_r(s)$  and  $SF_m(s)$

Similarly, the experimental frequency responses of  $D(s)$ ,  $T(s)$ , and  $S(s)$  are depicted in Figs. 24 and 25. Owing to narrow-band force rebalance control, there are two crossover frequencies appearing in the frequency-amplitude response of  $D(s)$  in  $f$  domain. Thus, according to classical control theory, there are two corresponding phase margins ( $PM_l$  and  $PM_r$ ), gain margins ( $GM_l$  and  $GM_r$ ), sensitivity margins ( $M_{sl}$  and  $M_{sr}$ ), and cutoff frequencies ( $f_{tl}$  and  $f_{tr}$ ), as marked in Fig. 24 and Fig. 25. They are interesting since we scarcely meet this case. After all, many control theory books

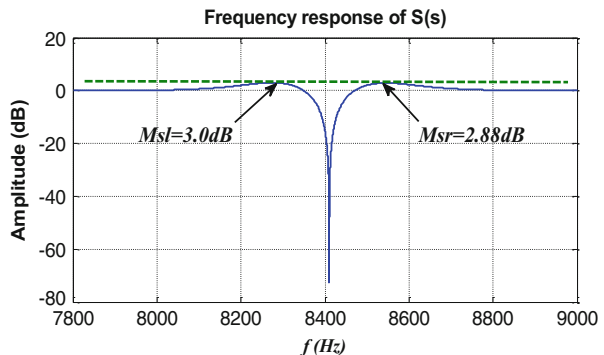
**Table 1** Stability indices of the gyroscope with closed-loop controlled sense mode

Type	$f$ domain		$f_r$ domain
Phase margin (deg)	$PM_l = 66.1$	$PM_r = 67.3$	$PM = 66.7$
Gain margin (dB)	$GM_l = 13.5$	$GM_r = 13.9$	$GM = 13.7$
Sensitivity margin (dB)	$M_{sl} = 3.0$	$M_{sr} = 2.88$	$M_s = 2.94$
Cutoff frequency (Hz)	$f_{il} = 8311$	$f_{ir} = 8505.1$	$f_i = 97.1$
Bandwidth (Hz)	$BW_r = 97.05$		$BW = 97.1$



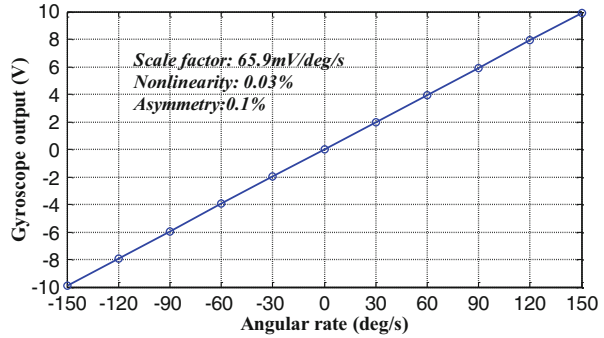
**Fig. 24** Frequency responses of  $D(s)$  and  $T(s)$

**Fig. 25** Frequency responses of  $S(s)$



usually show us that there is only one crossover frequency, one phase margin, one gain margin, one sensitivity margin, and one cutoff frequency in the frequency responses. Whatever, classical linear control theory is still suitable to analyze the stability. Although there is only one crossover frequency, one phase margin, one gain

**Fig. 26** The scale factor of the gyroscope with closed-loop controlled sense mode



margin, one sensitivity margin, and one cutoff frequency in  $f_r$  domain, the control loop is a force rebalance system, it had better study the stability in  $f$  domain, which helps us understand the system's robustness better.

The key stability indices listed in Table 1 indicate that the closed-loop system is stable and robust enough. Besides, the bandwidth  $BW_{lr}$  of  $T(s)$  is calculated to be about 97.05 Hz, which means that the force outside this narrow-band will never be balanced. Meanwhile, noises outside the bandwidth will be almost eliminated by the controller and filters. After closed-loop design,  $\omega_1$ ,  $\omega_2$ ,  $\omega_3$ , and  $k_p$  are finally set to be 0.1 rad/s, 50 rad/s, 5000 rad/s, and 400, respectively.

The mode-matching MEMS gyroscope with the closed-loop controlled sense mode achieves a scale factor of 65.9 mV/deg/s with nonlinearity about 0.03% and asymmetry about 0.1%, as shown in Fig. 26. From Fig. 27, the bias instability and angle random walk (ARW) are evaluated to be 0.68 deg/h and 0.028 deg/h<sup>1/2</sup>, respectively.

## Temperature Compensation

### Temperature Compensation Principle

As mentioned above,  $f_s$ ,  $f_d$ ,  $Q_s$ , and  $Q_d$  all vary with ambient temperature. Meanwhile, the parameters of capacitors, resistors, and amplifiers are also affected by ambient temperature. Hence, temperature compensation is very important to suppress the temperature sensitivity.

The schematic of an ANN temperature compensation system for a MEMS gyroscope is shown in Fig. 28. Given that  $f_d$  varies with temperature linearly, it can be utilized to temperature compensation for the drift induced by mechanical structure. Given that the temperatures of mechanical structure and circuit are a little different, a temperature sensor is adopted to measure the circuit's temperature  $T$ , which will be also applied to the compensation. Thus, an artificial neural network (ANN), such as BP neural network mentioned above, can be adopted to study the relationship between  $f_d$ ,  $T$ , and zero bias. Afterwards, the ANN temperature compensation model will be used to make a prediction and eliminate the bias

**Fig. 27** Allan variance graphs of the gyroscope with closed-loop controlled sense mode

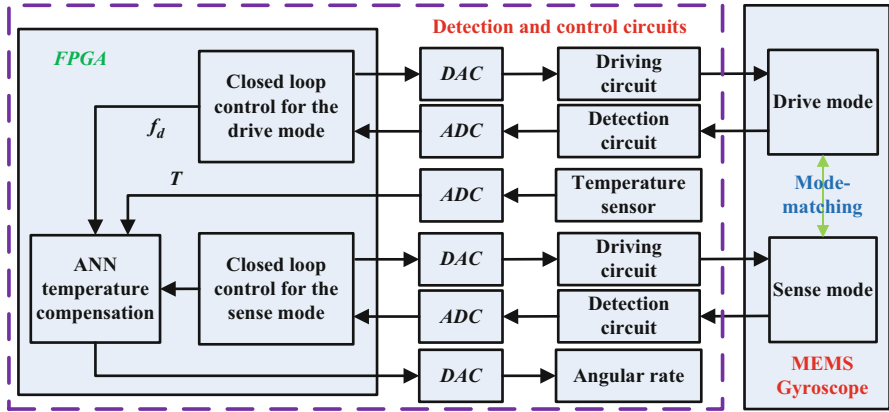
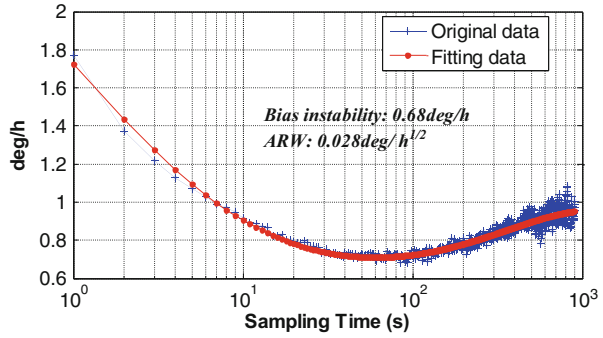


**Fig. 28** The schematic of an ANN temperature compensation system for a MEMS gyroscope

drift. The algorithm of a BP neural network has been introduced above, so we no longer repeat here.

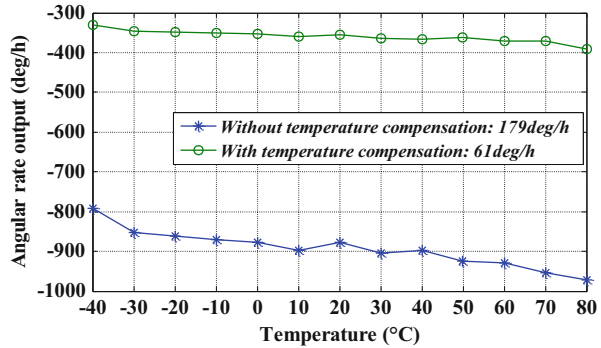
### Experimental Test

Figure 29 illustrates that zero bias varies with ambient temperature with or without temperature compensation. After compensation, the temperature sensitivity of bias drift over the temperature range from  $-40\text{ }^{\circ}\text{C}$  to  $80\text{ }^{\circ}\text{C}$  is improved to  $61\text{ deg/h}$  from  $179\text{ deg/h}$ , which indicates the proposed compensation method is feasible and effective.

### Conclusion

This chapter introduces the overview and fundamental operation principle of a MEMS vibratory gyroscope, meanwhile, some mature or novel methods of closed-loop control for the drive mode, mode-matching control, force rebalance control, and

**Fig. 29** Zero bias varies with ambient temperature with or without temperature compensation



temperature compensation are presented in detail. Besides, theoretical deduction, simulation, and experimental tests are combined tightly to make the proposed techniques understand easily. Actually, a MEMS gyroscope is a complicated system, and the relevant techniques are far more than those mentioned above.

## References

- Acar C, Shkel AM (2005) Structurally decoupled micromachined gyroscopes with post-release capacitance enhancement. *J Micromech Microeng* 15:1092–1101
- Ahn CH, Ng EJ, Hong VA et al (2015) Mode-matching of wineglass mode disk resonator gyroscope in (100) single crystal silicon. *J Microelectromech Syst* 24(2):343–350
- Aktakka E E and Najafi K (2016) A six-axis micro platform for in situ calibration of MEMS inertial sensors. *Proc MEMS 2016*, pp 243–246
- Askari S, Asadian MH, Kakavand K, Shkel AM (2006) Vacuum sealed and getter activated MEMS Quad Mass Gyroscope demonstrating better than 1.2 million quality factor. 2016 I.E. international symposium on inertial sensors and systems, pp 142–143
- Askari S, Asadian MH, Kakavand K, Shkel AM (2016) Vacuum sealed and getter activated MEMS Quad Mass Gyroscope demonstrating better than 1.2 million quality factor. 2016 I.E. international symposium on inertial sensors and systems, pp 142–143
- Cao HL, Li HS, Liu J et al (2016) An improved interface and noise analysis of a turning fork microgyroscope structure. *Mech Syst Signal Process* 70–71:1209–1220
- Casinovi G, Norouzpour-Shirazi A, Dalal M, Ayazi F (2016) Gyroscope sensing and self-calibration architecture based on signal phase shift. *Sensors Actuators A* 241:1–11
- Chen BD, Liu HZ, Wang HT et al (2011) Thermal shock induced nanocrack as high efficiency surface conduction electron emitter. *Appl Surf Sci* 257:9125–9128
- Chen F, Li XX, Kraft M (2016) Electromechanical sigma-delta modulators ( $\Sigma\Delta$ ) force feedback interfaces for capacitive MEMS inertial sensors: A review. *IEEE Sensors J* 16(17):6476–6495
- Cho J, Woo J K, et al. (2013) A high-Q birdbath resonator gyroscope (BRG). *Proc Transducers 2013*, pp 1847–1850
- Closkey RTM, Vakakis A, Gutierrez R (2001) Modelocalization induced by a nonlinear control loop. *Nonlinear Dyn* 3:221–236
- Cui J, Guo Z Y, Yang Z C, et al. (2011a) Electrical coupling suppressing for a microgyroscope using ascending frequency drive with 2-DOF PID controller. *Proc Transducers 2011*, pp 2002–2005
- Cui J, Guo ZY, Yang ZC et al (2011b) Electrical coupling suppression and transient response improvement for a microgyroscope using ascending frequency drive with a 2-DOF PID controller. *J Micromech Microeng* 21:095020

- Cui J, He CH et al (2012) Virtual rate-table method for characterization of microgyroscopes. *IEEE Sensors J* 12:2192–2198
- Dorf RC, Bishop RH (2005) *Modern control system*, 10th edn. Science Press, Beijing
- Fei JT, Xin MY (2012) An adaptive fuzzy sliding mode controller for MEMS triaxial gyroscope with angular velocity estimation. *Nonlinear Dyn* 70:97–109
- Flader IB, Ahn CH, Ng EJ et al. (2016) Stochastic method for disk resonating gyroscope mode matching and quadrature nulling. *Proc MEMS 2016*, pp 998–1001
- Fontanella R, Accardo D, Caricati E et al. (2016) An extensive analysis for the use of back propagation neural networks to perform the calibration of MEMS gyro bias thermal drift. *Proc Plans 2016*, pp 672–680
- Franssila S (2004) *Introduction to microfabrication*. Wiley, New York
- He CH, Zhao QC, Liu DC et al. (2013a) An automatic real-time mode-matching MEMS gyroscope with fuzzy and neural network control. *Proc Transducers 2013*, pp 54–57
- He CH, Zhao QC, Liu YX et al (2013b) Closed loop control design for the sense mode of micromachined vibratory gyroscopes. *Sci China Technol Sci* 56:1112–1118
- Lajimi SAM, Heppler GR, Abdel-Rahman EM (2017) A mechanical-thermal noise analysis of a nonlinear microgyroscope. *Mech Syst Signal Process* 83:163–175
- Lee A, Ko H et al (2008) Non-ideal behavior of a driving resonator loop in a vibratory capacitive microgyroscope. *Microelectron J* 39:1–6
- Li Z, Yang Z, Xiao Z et al (2000) A bulk micromachined vibratory lateral gyroscope fabricated with wafer bonding and deep trench etching. *Sensors Actuators A* 83:24–29
- Li J, Broas M, Makkonen J et al (2014) Shock impact reliability and failure analysis of a three-axis MEMS gyroscope. *J Microelectromech Syst* 23(2):347–355
- Li J, Mattila T, Vuorinen V (2015) MEMS reliability. Chapter 41 of *handbook of silicon based MEMS*. *Mater Technol* 744–763
- Liu XS, Yang ZC, Yan GZ et al. (2006) Design and fabrication of a lateral axis gyroscope with asymmetric comb-fingers as sensing capacitors. *Proc NEMS 2006*, pp 762–765
- Liu DC, He CH, Zhao QC et al (2014) Digital signal processing for a micromachined vibratory gyroscope based on a three dimensional adaptive filter demodulator. *Measurement* 50:198–202
- Makkonen J, Broas M, Li J et al. (2012) Reliability assessment of MEMS devices – a case study of a 3 axis gyroscope. *Proc ESTC 2012*, pp 1–8
- Pasquale GD, Soma A (2011) MEMS mechanical fatigue: effect of mean stress on gold microbeams. *J Microelectromech Syst* 20(4):1054–1063
- Pierron ON, Abnet CC, Muhlstein CL (2006) Methodology for low- and high-cycle fatigue characterization with kHz-frequency resonators. *Sensors Actuators A* 128:140–150
- Prikhodko IP, Trusov AA, Shkel AM (2013) Compensation of drifts in high-Q MEMS gyroscopes using temperature self-sensing. *Sensors Actuators A* 201:517–524
- Rombach S, Maurer M, Manoli Y (2015) Continuous-time lowpass and bandpass  $\Delta\Sigma$ -modulators for closed-loop readout circuits of capacitive MEMS gyroscopes. *Inertial Sensors and Systems*, pp 7–18
- Rombach S, Marx M, Nessler S et al (2016) An interface ASIC for MEMS vibratory gyroscopes with a power of 1.6 mW, 92 dB DR and  $0.007^\circ/s/\sqrt{\text{Hz}}$  noise floor over a 40 Hz band. *IEEE J Solid State Circuits* 51(8):1915–1927
- Rombacha S, Maurer M, Wendler D, Manoli Y (2015) Implementation of a modulated lowpass  $\Delta\Sigma$ -modulator for MEMS gyroscopes with low-power consumption and low sampling. *Procedia Eng* 120:832–835
- Senkal D, Askari S, Ahamed MJ et al (2014) 100K Q-factor toroidal ring gyroscope implemented in wafer-level epitaxial silicon encapsulation process. *Proc MEMS 2014*, pp 24–27
- Senkal D, Ahamed MJ, Askari S, Shkel AM (2015) Demonstration of 1 million Q-factor on microglassblown wineglass resonators with out-of-plane electrostatic transduction. *J Microelectromech Syst* 24(1):29–37
- Shao P, Tavassoli V, Mayberry CL, Ayazi F (2015) A 3D-HARPSS polysilicon microhemispherical shell resonating gyroscope: design, fabrication, and characterization. *IEEE Sensors J* 15(9):4974–4985

- Sharma A. (2007) CMOS systems and circuits for sub-degree per hour MEMS gyroscopes. Ph. D., Georgia Institute of Technology
- Sonmezoglu S, Alper SE, Akin T (2012) An automatically mode-matched MEMS gyroscope with 50Hz bandwidth. *Proc. MEMS 2012*:523–526
- Sonmezoglu S, Alper SE, Akin T (2014) An automatically mode-matched MEMS gyroscope with wide and tunable bandwidth. *J Microelectromech Syst* 23(2):284–297
- Tatar E (2010) Quadrature error compensation and its effects in the performance of fully decoupled MEMS gyroscope. MS. D., Middle East Technical University
- Tatar E et al (2012) Quadrature-error compensation and corresponding effects on the performance of fully decoupled MEMS gyroscopes. *J Microelectromech Syst* 21(3):656–667
- Torunbalci MM, Alper SE, Akin T (2015) Wafer level hermetic sealing of MEMS devices with vertical feedthroughs using anodic bonding. *Sensors Actuators A* 224:169–176
- Trusov AA, Prikhodko IP, et al. (2013) 1 PPM precision self-calibration of scale factor in MEMS Coriolis vibratory gyroscopes. *Proc Transducers 2013*, pp 2531–2534
- Vafanejad A, Kim ES (2015) Effect of diaphragm perforation on quality factor of hemispherical resonator gyroscope. *Proc Transducers 2015*, pp 27–30
- Xiao QJ, Li SY, Chen WY et al (2009) Fuzzy tuning PI control for initial levitation of micro-machined electrostatically levitated gyroscope. *Electron Lett* 45(16):818–819
- Yan JJ, He CH, Ge F et al (2011) Research of resonant frequency and quality factor test methods for high vacuum sealed microgyroscope based on LabVIEW. *Procedia Eng* 15:2566–2570
- Yang C, Li HS (2015) Digital control system for the MEMS tuning fork gyroscope based on synchronous integral demodulator. *IEEE Sensors J* 15(10):5755–5764
- Yang C, Li C, Zhang C (2010) The application of RBF neural network in the compensation for temperature drift of the silicon pressure sensor. *Proc Int ICCDA'10, Qinhuangdao*, 25–27 June 2010, vol 2, pp 434–437
- Yazdi N, Ayazi F, Najafi K (1998) Micromachined inertial sensors. *Proc IEEE* 86(8):1640–1659
- Yole Developpement 2015 (2016) <http://www.yole.fr/>
- Zhang QT, Tan ZF, Guo LD (2009) Compensation of temperature drift of MEMS gyroscope using BP neural network. *Proc Int ICIECS'09, Wuhan*, 19–20 Dec 2009, pp 1–4
- Zhang JM, He CH, Liu YX et al (2015) A novel scale-factor calibration method for a MEMS gyroscope based on virtual Coriolis force. *Proc NEMS 2015*, pp 58–62
- Zihajehzadeh S, Loh D, Lee TJ et al (2015) A cascaded Kalman filter-based GPS\_MEMS-IMU integration for sports applications. *Measurement* 73:200–210